1 *Review*

Chemical Diversity of Metal Sulfide Minerals and Its Implications for Prebiotic Catalysis

Yamei Li [1]*, Norio Kitadai [1] and Ryuhei Nakamura [1,2]*

[1] Earth-Life Science Institute, Tokyo Institute of Technology, 2-12-1 Ookayama,   Meguro-ku, Tokyo 152-8550, Japan;

[2] Biofunctional Catalyst Research Team, RIKEN Center for Sustainable Resource Science, 2-1 Hirosawa, Wako, Saitama 351-0198, Japan;

* Correspondence: yamei.li@elsi.jp; ryuhei.nakamura@ elsi.jp; Tel.: +81-3-5734-3414

Abstract: Prebiotic organic synthesis reactions catalyzed by Earth-abundant metal sulfides are key processes for understanding the evolution of biochemistry from inorganic molecules, yet the catalytic functions of sulfides have remained poorly explored in the context of the origins of life. Past studies on prebiotic chemistry have mostly focused on a few types of metal sulfide catalysts, such as FeS or NiS, which form limited types of products with inferior activity and selectivity. To explore the potential of metal sulfides on catalyzing prebiotic chemical reactions, here, the chemical diversity (variations in chemical composition and phase structure) of 304 natural metal sulfide minerals in a mineralogy database was surveyed and approaches to rationally predict the catalytic functions of metal sulfides are discussed based on advanced theories and analytical tools of electrocatalysis such as proton-coupled electron transfer, structural comparisons between enzymes and minerals, and in-situ spectroscopy. To this end, we introduce a model of geo-electrochemistry driven prebiotic synthesis for chemical evolution, as it helps us to predict kinetics and selectivity of targeted prebiotic chemistry under "chemically messy conditions". We expect that combining the data-mining of mineral databases with experimental methods and theories developed in the field of electrocatalysis will facilitate the prediction and verification of catalytic performance under a wide range of pH and Eh conditions, and aid in the rational screening of mineral catalysts involved in the origins of life.

Keywords: Origins of life; prebiotic chemistry; mineral catalysis; sulfide minerals; mineral diversity; density functional theory; electrocatalysis

1. Introduction

The origins of life on Earth and Earth-like planets are generally envisioned as having started from abiotic syntheses of basic building blocks requisite for metabolism and replication [1–5]. Metal sulfides have been proposed as key players in these prebiotic processes in several scenarios, such as the "iron–sulfur world" by Wächtershäuser [6,7], the "iron–sulfur membrane model" by Russell and Hall [5,8,9] and more recently by Lane and Martin [10], and the "geoelectrochemistry driven origin of life" by Nakamura, Yamamoto [11–16], and Barge [17–19]. Metal sulfides are ubiquitous in reducing environments, including sulfidic ores [20,21], deep-sea hydrothermal vent deposits [8,22–24], sulfide-rich euxinic sediment environments (e.g., black sea) [25–27], and in black shale [28–30]. In deep-sea hydrothermal vent environments, where massive sulfide deposits are produced, many transition metals are dissolved and concentrated in hydrothermal fluids mainly as chloride complexes [20,21]. The generally low solubility of metal sulfides possibly limited the bio-availability of metal ions in the early ocean and has led to the assumption that the availability of metal ions in the ocean may have constrained metabolic pathways in early life [31–33].

Deep-sea hydrothermal systems associated with the serpentinization of ultramafic rocks are among the most plausible geological settings for life to have originated [8,10,11,13,15,16,34,35]. The temperature, pH, and chemical composition differences between hydrothermal fluid and seawater generate a steep redox gradient across the sulfide-rich vent rocks, thereby serving as the driving force for prebiotic chemistry [5,8,9]. In addition, the generation of a chemical potential gradient across electrically conductive metal sulfide minerals provides a continuous and uni-directional supply of high-energy electrons from the inside of the vent to the outside of the rock wall, as has been proposed based on the electrochemical analysis of hydrothermal vent minerals [15,17,19] and the electrochemical potential mapping of deep-sea hydrothermal fields [11,15,16]. In this environment, the high-energy electrons continuously supplied by the natural geoelectrochemical reactor trigger CO_2 reduction to form CO and CH_4 and nitrate and nitrite reduction to form NO, N_2O, and NH_3, as demonstrated in recent laboratory investigations [12–14,36]. Under the continuous flow of electrical current from a hot, reductive hydrothermal fluid to cold seawater, the ocean-vent interface is ideal for prebiotic chemistry, as a number of key organic molecules, including α-keto acids, amino acids, and oligonucleotides, involved in life's origins are unstable at high temperatures [5,8]. In addition, the unique nano- and micro-scale structures of metal sulfide minerals in hydrothermal vent environments may have promoted the concentration and organization of the synthesized molecules, preventing them from diffusing into seawater [37,38].

The thermo- and electro-catalytic properties of metal sulfides are critical for understanding how the pH, temperature, and Eh disequilibria between hydrothermal fluids and seawater trigger prebiotic organic synthesis. In mineralogy, metal sulfides have been studied mainly with respect to crystallography, thermodynamic and high pressure phase transition, air stability, electric and magnetic properties, trace element incorporation, and mineral conversion [39,40]. Their thermo-catalytic activities towards hydrogenation, hydrodesulfurization and hydrodenitrogenation reactions have also been studied under gas-phase, high temperature conditions in petrochemistry since the 1920s [41,42]. However, the thermal and electrochemical catalysis of metal sulfides remain poorly explored in the context of the origin of life, particularly under simulated hydrothermal vent conditions.

To synthesize macromolecules (phospholipids, oligo-nucleotides, and peptides) and their respective building blocks (fatty acids, glycerol, ribose, nucleobases, nucleotides, and amino acids) from simple molecules (CO_2, N_2, NO_3^-/NO_2^-, and H_2) to form a complex prebiotic chemical network, efficient mineral catalysts must be identified, which requires extensive screening efforts. Although several studies have used sulfides as catalysts for abiotic carbon and nitrogen fixation, and peptide bond formation [12–14,36,43–48], limited types of organic products were typically formed and had activities and selectivity that were generally lower than those found in contemporary biological systems. These problems suggest that new types of earth-abundant mineral catalysts that function efficiently under geologically relevant conditions are needed for prebiotic synthesis.

Numerous minerals are identified in natural environments yearly, contributing to a huge library of mineral catalysts, and the number of unknown minerals awaiting discovery is predicted to be even larger [49,50]. As will be presented in this review, natural metal sulfides in mineralogy databases show marked variation in chemical composition, crystal structure and metal/sulfur valence states, and therefore have the potential for a wide variety of catalytic functions. However, prebiotic experiments conducted to date have rarely taken into account these diversities, and have typically only used a limited number of single-metal sulfides, such as FeS and NiS, with a few exceptions [12,13,51], most likely due to the lack of the general principle to predict the catalytic function of natural mineral samples. Notably, in the field of heterogeneous catalysis, earth-abundant transition metal sulfides have attracted keen attention as cost–effective catalysts for energy conversion applications [52]. In particular, the hydrogen evolution reaction, hydrogen oxidation, CO_2 reduction reaction, nitrate/nitrite reduction, and N_2 reduction catalyzed by metals, metal oxides, and metal sulfides have been analyzed catalytically to identify the structural and electronic features of intermediates involved in the targeted reactions and determine the reaction pathways. Moreover, the application of the advanced theory of proton-coupled electron transfer allows prediction of how the

97 activity and selectivity of prebiotic catalysts are potentially influenced by solution pH and Eh [53–
98 55].

99   In the present review, we highlight the significance of the chemical diversity and complexity of
100 natural metal sulfides for facilitating prebiotic chemical evolution and propose rational approaches
101 for screening mineral catalysts from mineralogy databases. First, prebiotic synthesis experiments
102 conducted to date using sulfides as catalysts will be summarized and the chemical diversity of metal
103 sulfides in the mineralogy database will be surveyed with emphasis on Cu, Co, Fe, Mn, Mo, Ni, V,
104 and W as the metal components, as these elements contain multiple accessible oxidation states and
105 are involved in biological redox reactions with sulfur as pervasive ligands. Transition metal sulfides
106 have been proposed to have evolutionary significance as protoenzyme catalysts of enzyme-mimetic
107 reactions [4,14,56,57]. Further, the structure–function relationship of metal sulfides is discussed based
108 on material and catalysis engineering research findings. In addition, studies on metal sulfides with
109 well-defined crystal phases, chemical composition, and defect structures are reviewed. Finally,
110 theoretical and experimental approaches for probing structure-function relationships and predicting
111 heterogeneous catalytic properties are introduced. By presenting this integrated information, we
112 hope to promote the screening and performance prediction of sulfide catalysts in prebiotic processes
113 that preceded the origin of life.

114 **2. Catalysis on metal sulfides relevant to prebiotic chemistry**

115 *2.1. Thermal Catalysis on Metal Sulfides*

116   Experiments on sulfide-promoted prebiotic reactions reported to date can be divided into two
117 categories: non-catalytic (stoichiometric) and catalytic. A representative example of a non-catalytic
118 process is associated with Wächtershäuser's proposal of an "iron–sulfur world", where FeS oxidation
119 from mackinawite to pyrite (FeS + $H_2S \rightarrow FeS_2 + 2H^+ + 2e^-$) provides reducing energy for organic
120 syntheses. Huber and Wächtershäuser demonstrated that the reductive amination of α-keto acids to
121 the corresponding α-amino acids (e.g., pyruvate + NH_3 + $2H^+$ + $2e^- \rightarrow$ alanine + H_2O) occurs on
122 freshly precipitated FeS, which was simultaneously oxidized to Fe^{3+} [48]. Interestingly, the reaction
123 showed a strong metal specificity, as replacing FeS with Ag_2S, CoS, Cr_2S_3, CuS, MgS, MnS, NiS, or
124 ZnS did not result in amino acid formation. Heinen and Lauwers showed that CO_2 was reduced to
125 alkane thiols and CS_2 in a serum bottle containing FeS, H_2S, water, and pure CO_2 gas or a mixture of
126 N_2 and CO_2 gases [58], with the formation of pyrite and H_2 as byproducts.

127   In addition to carbon fixation, ammonia serves as a reduced active nitrogen-bearing molecule
128 that is involved in the synthesis of amino acids, nucleotides, and other important N-containing
129 macromolecules. Therefore, prebiotic ammonia synthesis has been investigated by reducing either
130 nitrate/nitrite anions or di-nitrogen. FeS can reduce nitrate and nitrite to ammonia in an acidic
131 solution (pH 4) with the simultaneous oxidation of FeS to Fe_2O_3 [44]. The reaction was inhibited
132 effectively in the presence of either Cl^-, SO_4^{2-} or $H_2PO_4^-$, likely owing to the low binding affinity of
133 nitrate on the catalyst surface. Brandes et al. [59] reported that pyrite and pyrrhotite reduce nitrate
134 and nitrite to ammonia at a high yield (21%~89%) at temperatures between 300 and 700 ^{o}C and
135 pressures of 0.1-0.4 GPa. These researchers also observed that $Fe/H_2O/N_2$ or $Fe_3O_4/HCOOH/N_2$
136 systems reduce dinitrogen to ammonia at optimal temperatures of 700 and 500 ^{o}C, respectively, and
137 a pressure of 0.1 GPa, albeit with a lower yield than that obtained from nitrate/nitrite reduction [59].
138 Based on these results, an oceanic or hydrothermal source for reduced nitrogen on early Earth was
139 proposed. Dörr et al. [60] demonstrated the fixation of N_2 to ammonia on freshly precipitated FeS
140 using H_2S as a reductant under milder conditions (atmospheric nitrogen pressure and temperatures
141 of 70–80 ^{o}C) with a yield of 0.1%. The Fe-S cluster-like surface moieties, which resemble the active
142 center of FeMoS nitrogenase, were proposed to play a key role for activating N_2.

143   For catalytic conversions of carbon and nitrogen-bearing molecules, Huber and Wächtershäuser
144 reported that FeS, NiS, and (Fe,Ni)S provide favorable surface sites for activated thioester (CH_3-CO-
145 SCH_3) formation from CO and CH_3SH [45] and for amino acid polymerization via CO and H_2S
146 condensation to COS [47]. The former reaction resembles that found in the reductive acetyl-coenzyme

147   A pathway, in which Ni and Fe centers are responsible for binding CH_3SH and CO, respectively.
148   Cody et al. [61] examined the condensation of alkylthiol (RSH; R = nonyl group) and CO under high
149   temperature (250 °C) and pressure (200 MPa) conditions in the presence of FeS and detected a small
150   amount of pyruvate formation. FeS was inferred to activate pyruvate synthesis by forming a
151   carbonylated iron sulfur complex ($Fe_2(RS)_2(CO)_6$). Further, Cody et al. [51] assayed several nickel,
152   cobalt, iron, copper, and zinc containing sulfides for hydrocarboxylation under the same high
153   temperature and pressure conditions and found that carboxylic acid was synthesized via carbonyl
154   insertion at metal-sulfide-bound alkyl groups. With the exception of CuS, all of the metal sulfides
155   promoted hydrocarboxylation. Because many transition metal complexes, including tertiary
156   phosphate complexes of Co^{2+}, Fe^{2+}, Mo, and Ni^{2+}, $CH_3Mn(CO)_5$ [62–64], are capable of mediating
157   carbonyl insertion, similar chemical reactions can potentially proceed on various types of metal
158   sulfides. In presence of FeS, Novikov et al.[65] demonstrated the reduction of ketones to alcohols and
159   aldol condensation with pyruvate, H_2, H_2S as the starting materials at more moderate temperatures
160   (25–110 °C). These reactions were considered to be important because of their participation in extant
161   metabolic pathways. Notably, addition of NH_4Cl induced the reductive amination to generate alanine.

162   *2.2. Electrocatalysis on metal sulfides*

163   Recently, a model of geo-electrochemistry driven organic synthesis was proposed based on the
164   detection of electrical current flow in natural deep-sea hydrothermal fields [11,16] and demonstration
165   of the relevant organic syntheses in a laboratory setting [12–14,17,19,36]. The temperature, pH, and
166   chemical composition differences between hydrothermal fluid and seawater generate a steep redox
167   gradient across sulfide-rich vent rocks (Figure 1). This unique geoelectrochemical environment
168   results in continuous and unidirectional electron flow from the internal hydrothermal fluid to the
169   external chimney rock wall by coupling the oxidation of H_2 or H_2S in the hydrothermal fluid with the
170   reduction of species, such as H_2O, CO_2, and nitrate/nitrite, in seawater. The wide range of redox
171   potentials and pHs in this environment control the kinetics and selectivity of target reactions even
172   under chemically messy conditions, circumventing their lack of stereoselectivity seen in modern
173   enzymatic systems [12–14]. As the reaction energetics and kinetics are dependent on multiple
174   parameters (Eh, pH, and T), the distribution of products can be tuned based on the wide variation of
175   possible geochemical environmental parameters, which have the potential to be rationally predicted
176   based on the theory of proton-coupled electron-transfer [53–55]. In addition, if the electrochemical
177   fuel cell model (two-container model for prebiotic reactions; Figure 1) is applied to prebiotic reactions,
178   even strong endothermic reactions can be initiated, as the pH (ΔpH) and temperature gradients (ΔT)
179   across the electrically conductive, yet thermally insulative vent wall [66] can be used to generate high-
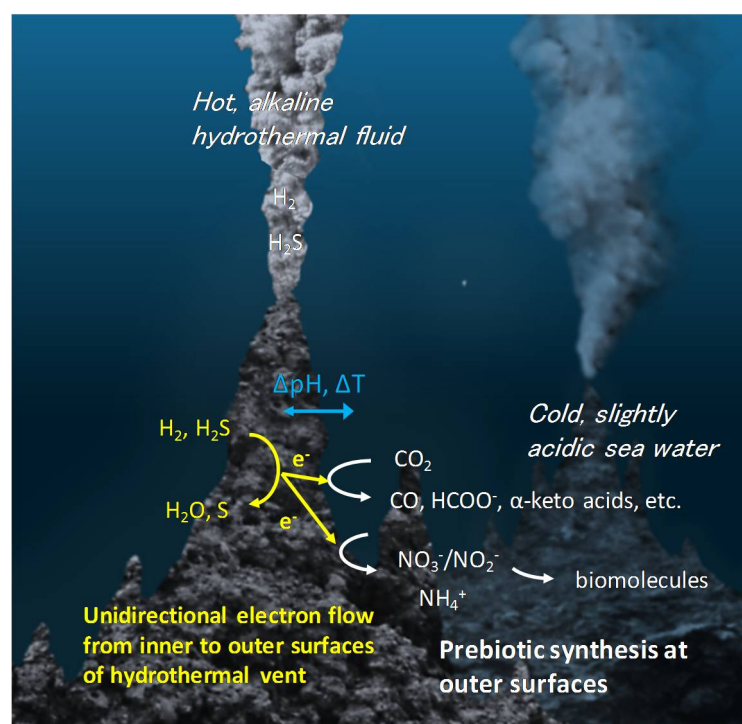180   energy electrons at cold, ocean-vent interfaces [11–15,67].
181

Figure 1. Model of geoelectrochemical prebiotic synthesis for chemical evolution. In deep-sea hydrothermal vents, electrons generated from the oxidation of H_2 and H_2S molecules in the hydrothermal fluids flow towards the seawater-rock interface through the porous, conductive metal sulfide chimney mineral wall. The reduction of molecules, such as CO_2, NO_3^-, NO_2^-, in the seawater is catalyzed by metal sulfides to generate various types of organic building blocks, which further undergo condensation or polymerization to generate bio-essential molecules and polymers.

Based on the electrochemical fuel cell model, Yamaguchi et al. [13] demonstrated the electrocatalytic reduction of CO_2 to CO and CH_4 on greigite (Fe_3S_4) under simulated alkaline hydrothermal vent conditions. As CO_2 reduction will not proceed without overcoming the high energetic barrier associated with the first electron uptake step (–1.9 V vs. SHE at pH 7) and also competes with the thermodynamically and kinetically more favorable reduction of protons to form H_2, the Faraday efficiency for CO production ($CO_2 + 2H^+ + 2e^- \rightarrow CO + H_2O$) is low (< 0.02% in total at –1.3 V vs. SHE) at pH 5.5. However, by doping FeS with Ni to form $FeNi_2S_4$ (violarite), the CO_2 electroreduction selectivity is enhanced by ~ 85-fold concurrently with a lowered onset potential (–0.5 V vs. SHE, pH 5.5). CO_2 reduction activity is further enhanced by modifying Ni-doped FeS catalyst with amine compounds [13]. Yamaguchi et al. have also found that the onset potential for CO_2 reduction on Ni-doped FeS catalyst is ~ 180 mV more negative than the redox couple of H^+/H_2 at pH 5.5, suggesting that a naturally occurring proton motive force (PMF), which is equivalent to a 3~4 pH gradient, is sufficient to initiate CO_2 reduction to form CO when the hydrothermal fluid pH is higher than 9. Note that violarite resembles the $NiFe_4S_4$ active center of carbon monoxide dehydrogenase, and the amine species further enhance the CO_2 reduction activity, similar to the peptide amine group surrounding the enzymatic active center (ligand-assisted catalysis). Amine-induced enhancement was associated with the ability of violarite to donate electrons to the anti-bonding π * orbital of CO_2, which is essential for the efficient electrochemical activation of CO_2 [67].

A study by Kitadai et al. [12] using various single-metal sulfides (Ag_2S, CdS, CoS, CuS, FeS, MnS, MoS_2, NiS, PbS, WS_2, and ZnS) demonstrated that CdS and Ag_2S function as excellent CO production catalysts ($CO_2 + 2H^+ + 2e^- \rightarrow CO + H_2O$). The Faraday efficiency was as high as 40% on CdS at ≤–1.0 V (vs. SHE) at pH 5.5–6. The selective production of CO from CO_2 by CdS and Ag_2S is remarkable, because even though CO is frequently used as a carbon source for organic synthesis through thermocatalysis, CO is considered to have been present in only trace amounts in the Hadean atmosphere [68]. However, CO_2 fixation into C_2–C_3 compounds, such as acetate and pyruvate, has

214   rarely been demonstrated by metal sulfide materials under electrochemical conditions. One exception
215   was reported by Roldan et al. [36], who demonstrated CO_2 reduction on highly faceted greigite
216   nanoparticles into a series of C_1–C_3 compounds, including formic acid, acetic acid, methanol, and
217   pyruvic acid. In contrast to the reports by Yamaguchi and Kitadai [12,13], Roldan et al. [36] cycled
218   the electrode potential continuously during electrochemical CO_2 reduction between 0.2 and -0.8 V vs.
219   SHE (pH 6.5) at a slow rate (1 mV s^{-1}), which may have promoted the formation of C-C bonds.

220   In the geo-electricity driven prebiotic catalysis model, trace metal elements, such as Mo and W,
221   could have played a significant role in prebiotic chemistry, as the continuous supply of electrons to
222   the metal sites maintain the catalytic cycle. For example, Li et al. [14] demonstrated that molybdenum
223   sulfide (MoS_2) and Mo-doped greigite serve as electrocatalysts for reducing nitrate and nitrite into
224   ammonia, It was found that in the presence of anions, such as phosphate, sulfate, iron sulfide impairs
225   nitrate reduction, similar to the inhibition observed on FeS by Summers et al. [44]. In contrast,
226   molybdenum sulfide can catalyze both nitrate and nitrite reduction over a wide pH range (pH 3~11)
227   in the presence of phosphate and sulfate anions. In a neutral medium using molybdenum sulfide as
228   the catalyst, ammonia was generated through nitrate reduction at an onset potential of 0 V vs. RHE
229   (reversible hydrogen electrode). At more positive potential regions (0.6~0 V vs. RHE), not only
230   ammonia, but also strong oxidants such as nitric oxide (NO) and nitrous oxide (N_2O) are generated
231   from nitrite and show a potential-dependent distribution. This result suggests that the proton motive
232   force is not required for ammonia synthesis. Notably, greigite doped with 5 atom % Mo efficiently
233   activates nitrite reduction, suggesting that even at trace amounts, Mo can function as a catalytic site.

234   As a short summary, previous prebiotic chemical syntheses conducted using metal sulfides as
235   the catalysts showed that in addition to iron sulfide, other transition metal sulfides can potentially
236   function as C and N fixation catalysts with even higher activity than iron sulfides. The catalytic
237   performance of CO_2 reduction varies largely depending on the doping elements, crystal size, and
238   surface structure of greigite, as well as the pH and Eh conditions [12,13,36]. Therefore, due to the
239   chemical diversity of metal sulfides, in addition to the influence of pH and Eh on catalytic activity,
240   suitable catalysts with optimized activity can be potentially identified by screening reaction
241   conditions and mineralogy databases. Effective stoichiometric C and N fixation reactions require an
242   abundant source of electrons, a condition that suggests that Fe^{2+}-containing species were the main
243   reductants in the early ocean. Nevertheless, if geoelectrical currents serve to supply energy as a
244   trigger of prebiotic catalysis, even trace amounts of metal elements can continuously catalyze the
245   reaction [14].

246   The above rationale and experimental evidence suggests that prebiotic metal sulfide catalysts
247   should be screened not only based on the abundance of the metal, but also the electrocatalytic activity.
248   In comparison to iron sulfides, the electrochemical and electrocatalytic properties of transition metal
249   sulfides and their mixtures remain poorly understood, with a limited number of studies conducted
250   to date [12,13,51]. Proposed reaction mechanisms of these compounds are based on their resemblance
251   with similar enzymatic processes, such as those mediated by carbon monoxide dehydrogenase [13],
252   acetyl-CoA synthase [51,61], and nitrogenase [60], although no sufficient spectroscopic evidence
253   and/or valence state information has been provided. The underlying reaction mechanisms should
254   therefore be investigated in more detail for guiding catalyst screening based on functional, rather
255   than structural, relevance to well-characterized enzymes.

256   **3. Chemical diversity of metal sulfides in mineralogy libraries**

257   As the coordination and electronic structure of mineral surfaces largely determines catalytic
258   activity, here we evaluate the chemical diversity of naturally occurring metal sulfide minerals to aid
259   in the screening and identification of suitable prebiotic sulfide catalysts. A special emphasis was
260   placed on the sulfides containing Co, Cu, Fe, Mn, Mo, Ni, V and/or W, as they are well-known redox-
261   active elements and present in the active centers of enzymes catalyzing carbon and nitrogen
262   conversions, such as those mediated by carbon monoxide dehydrogenase (Fe, Ni, Cu and Mo), a
263   cobalt cobalamin cofactor for methyl transfer in acetyl-CoA synthase (Co), nitrogenase (Mo, V and
264   Fe), nitrate reductase (Mo), nitrite reductase (Fe, Cu, and Mo), formate dehydrogenase (Mo and W),

aldehyde oxidoreductase (Mo and W), and nitrous oxide reductase (Cu). In these enzymatic processes, these transition metals switch oxidation states for charge accumulation, coordinate to a variety of substrates and intermediates, and also catalyze enzymatic redox reactions involving simple inorganic molecules, such as H_2, AsO_2^-, S_x^{n-}, as substrates, which function as coupling reactions for energy conversion and conservation. Sulfur is a pervasive ligand in the first coordination sphere of the enzymatic cofactors, although cobalt cobalamin is an exception, as tetrapyrrole serves as the ligand. The ubiquitous role of metals and sulfur in metabolic processes has led to the hypothesis that metal sulfides worked as "proto-enzymes" for prebiotic organic syntheses, and sustained the continuous chemical evolution toward functioning in complex biochemical systems [4,14,56,57].

Among the 5,327 mineral species discovered to date (as officially listed by the International Mineralogical Association (IMA); http://rruff.info/ima/, as of May 18th, 2018), 304 metal sulfides contain Co, Cu, Fe, Mn, Mo, Ni, V and/or W with 135,434 species-locality pairs. We evaluated the diversity and distribution of these metal sulfides based on the following criteria:

1) *Locality frequency*. This parameter reflects the availability of minerals in natural environments. Although detection limits and metal-specific biases reflecting the metal's economic value may exist, an estimate of the probability of natural occurrence is useful for evaluating the feasibility of mineral-promoted prebiotic reactions.

2) *Multiple metal composition*. Naturally observed metal sulfides are commonly coupled to more than one transition metal and occasionally exhibit ternary compositions. Because cation substitutions and the presence of dual metal surface sites influence catalytic activities of minerals, as described in Sections 2.2, 4 and 5, metal-specific behaviors and tendency to form multiple compositions are important factors for screening potential mineral catalysts.

3) *Crystal structure and valence state of dominating elements*. These two properties, particularly the valence state, control the electronic characteristics of the mineral. Valence state information is available for 89% of the localities of metal sulfides in the database (http://rruff.info/ima/).

3. 1. Distribution of transition metal sulfides

The locality count indicates the frequency that a certain mineral will be found within a wide range of geological localities. Although this parameter partially reflects the natural occurrence probability within the ability of human detection, it is useful for evaluating the relative importance of the minerals as geochemical catalysts. Among the 304 metal sulfides considered, Fe-containing sulfides dominate the library (Figure 2). Pyrite ($Fe^{2+}S^-_2$) is the most frequently found species, followed by chalcopyrite ($Cu^+Fe^{3+}S^{2-}_2$), pyrrhotite ($Fe^{2+}_5Fe^{3+}_2S^{2-}_8$), arsenopyrite ($Fe^{2+}(AsS)^{2-}$), molybdenite ($Mo^{4+}S^{2-}_2$), chalcocite ($Cu^+_2S^{2-}$), marcasite ($Fe^{2+}S^-_2$), bornite ($Cu^+_5Fe^{3+}S^{2-}_4$), and tetrahedrite ($Cu^+_{10}Cu^{2+}_2Sb^{3+}_4S^{2-}_{13}$). The locality counts of these minerals exceed 5,000 and together, these minerals comprise ~80% of the sulfide minerals discovered to date. According to deep-time analysis, the nine most frequently observed minerals may have been present since the middle Archean eon (~ 3,500 Ma) or perhaps even earlier, although directly dated sulfides are rare.

Among transition metal sulfide species in the library, ~ 39% (119 species) contain iron, and are found in ~ 74% of localities (Figure S1), suggesting that iron was a pervasively occurring element during sulfide mineral formation. Co, Mn, Mo, W and V are mostly seen in Fe-free sulfides (>93% relative to the respective sulfides' locality counts), whereas Cu and Ni show a high tendency to coexist with Fe. Cu-Fe- and Ni-Fe-containing sulfides are seen in 59% and 45% of localities of Cu- and Ni-sulfides, respectively, and exhibit structural variations accounting for 32% and 42% of the total number of Cu- and Ni-sulfide species, respectively. Nevertheless, Fe-free Cu and Ni single-sulfides exhibit high locality counts (24,085 and 2,848, respectively), among which chalcocite ($Cu^+_2S^{2-}$) and millerite ($Ni^{2+}S^-$) are particularly prevalent (5,520 and 1,007 localities, respectively). Thus, although Cu and Ni tend to easily incorporate into Fe-bearing sulfides, their Fe-free sulfide forms are also ubiquitous. Please refer to Figures S1–S8 for more information regarding the spatial distribution and compositional diversity of metal sulfides.
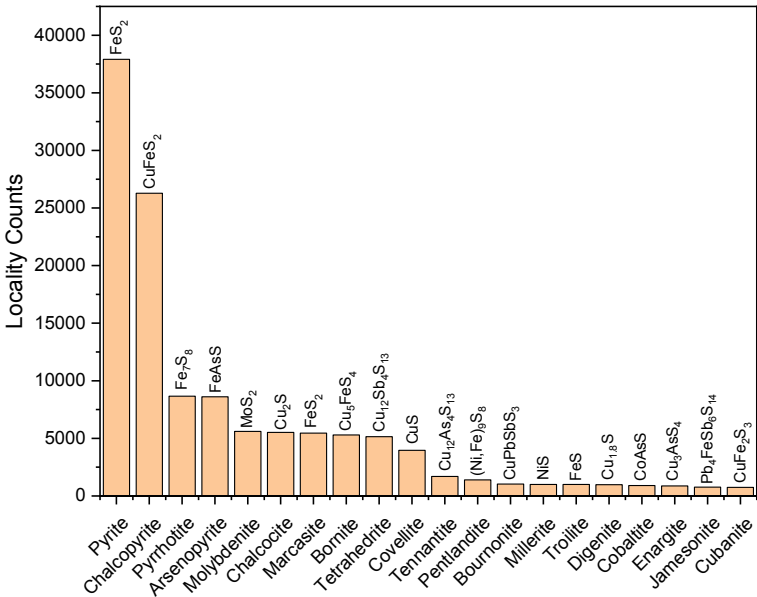
Figure 2. Metal sulfide distribution in natural environments. The 20 most frequently observed species are ranked in order of locality counts. The chemical composition of each species is shown.

3. 2. Single-metal sulfides

Single–metal sulfide minerals have been mainly investigated as key prebiotic catalysts [12,14,36,44–48]. By studying this family of minerals, their intrinsic metal–specific properties can be derived and compared, as was shown by Kitadai et al. [12] through the intensive screening of catalysts for CO_2 fixation. Single-metal sulfides of Fe, Cu, and Ni show marked variations in crystal structure, chemical composition and metal/sulfur valence states. Among 45 Fe single-metal sulfides (Figure 3), two pairs of polymorphs are present with the chemical compositions of FeS_2 (pyrite and marcasite) and FeS (troilite and keilite). Pyrite and marcasite have indirect band gaps of 0.7 and 0.4 eV, respectively [69]. Orthorhombic marcasite exhibits an anisotropic property that results in a unique sulfur surface site (sulfur trimers) on a specific surface orientation [70]. In contrast to pyrite on which S^{2-} is firstly oxidized, the sulfur trimer species on marcasite are most easily oxidized.

Fe single-metal sulfides in 91% of localities have valence state information. Sulfides having Fe^{2+} alone dominate the mineral family (84.86%), followed by those containing both Fe^{2+} and Fe^{3+} (15.12%), and by three sulfides that only contain Fe^{3+} (0.02%). Sulfides composed of a mixture of Fe^{2+} and Fe^{3+}, such as pyrrhotite ($Fe^{2+}_5Fe^{3+}_2S^{2-}_8$) and greigite ($Fe^{2+}Fe^{3+}_2S^{2-}_4$), typically exhibit magnetic properties [71–73].

Cu-, Co-, and Ni-single sulfides also display diverse chemical and physical properties (Figures S9-11). As many as 119 species were identified in Cu single-metal sulfides, of which 27 species have valence state information (73% relative to the locality counts of Cu single-metal sulfides). In addition, 18 species contain only Cu^+ (59%), four (tetrahedrite, tennantite, famatinite, and kuramite) are formed from Cu^+ and Cu^{2+} (40%), and the remaining 5 species possess only Cu^{2+} (<0.6%). The percentages in parentheses represent the respective mineral distributions relative to the locality counts of Cu single-metal sulfides with valence state information.

Co single-metal sulfides form 10 different structures, including five Co^{3+}-sulfides with two sulfosalt polymorphs, $Co^{3+}(AsS)^{3-}$ (cobaltite and alloclasite) and $Co^{3+}(SbS)^{3-}$ (willyamite, costibite, and paracostibite). Linnaeite ($Co^{2+}Co^{3+}_2S_4$) is the only species having a mixed valence state. The environmental distributions of Co^{3+}-, Co^{3+} plus Co^{2+}-, and Co^{2+}-sulfides are 78.93%, 18.47%, and 2.59%, respectively, relative to the total locality counts of Co single-metal sulfides.

For Ni single-metal sulfides, the valence state of Ni is always +2, with the exception of polydymite, which has both Ni^{2+} and Ni^{3+} ($Ni^{2+}Ni^{3+}_2S^{2-}_4$).

In Mn, Mo, and W single–metal sulfides, the valence states of metals are conserved, with only Mn^{2+}, Mo^{4+}, and W^{4+} being observed.

350   For V single-metal sulfides, three species are known (patrónite (VS_4), colimaite (K_3VS_4), and
351   yushkinite ($(Mg,Al)(OH)_2VS_2$)), in which the valence state of vanadium is +4 or +5. The occurrence of
352   these species in natural environments is rare, and V-bearing sulfides are typically found as Cu–V
353   binary forms (95% in terms of locality).

354   Generally, metals with low valence states predominate the library of metal sulfides, with the
355   exception of Co, allowing these minerals to act as an electron source or a catalytic center for charge
356   accumulation during redox conversion. In addition, sulfur with a –1 valence state, which typically
357   exists as a disulfur $(S_2)^{2-}$ ligand, can act as an electron-accepting site, and thus has the potential to be
358   involved in redox catalysis. The participation of not only metal sites, but also sulfur ligands, during
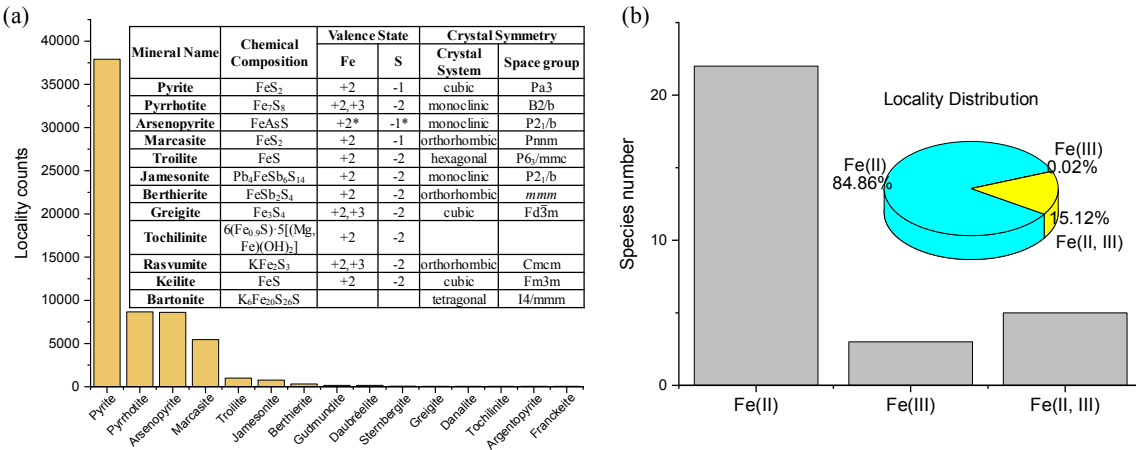359   redox catalysis has been extensively reported and will be discussed in Section 4.3.

Figure 3. (**a**) Distribution and chemical diversity (chemical composition, Fe/S valence states, and
crystal symmetry) of Fe single-metal sulfides. (**b**) Relative abundances and locality distribution of
Fe^{2+}-, Fe^{3+}-, and Fe^{2+} plus Fe^{3+}-sulfides. Note that the valence state of arsenopyrite ($Fe^{3+}(AsS)^{3-}$) in the
RRUFF mineral database is examined as ($Fe^{2+}(AsS)^{2-}$) in this review based on electric spectroscopic
observations [74,75].

3. 3. Binary- and ternary-metal sulfides

380   As described in Section 2.2, the doping of a secondary metal in iron sulfide can enhance the
381   activity and selectivity of CO_2 reduction [13]. Sulfides with binary metal composition can thus
382   potentially serve as superior catalysts to their single-metal counterparts. In addition, as binary metal
383   sites are present in several extant enzymatic systems, such as Ni-S-Fe hydrogenase, Ni-S-Fe carbon
384   monoxide dehydrogenase (CODH), Mo-S-Cu CODH, Fe-S-Mo nitrogenase, and Fe-S-V nitrogenase,
385   it has been suggested that binary metal centers can synergistically function as Lewis acid and base
386   sites for facilitating catalysis. For example, Fe and Ni bind CO_2 in a bidentate mode via O and C atoms,
387   respectively [76].

388   Cu-bearing binary sulfides exhibit 193 structures among 58,932 localities and include 52 species
389   of Cu-Fe binary sulfides (59% in terms of locality) (Table S1). Calcopyrite ($Cu^{1+}Fe^{3+}S^{2-}_2$) and bornite
390   ($Cu^{1+}_5Fe^{3+}S^{2-}_4$) are the most prevalent forms in this category. Sulfides with Fe and Cu as substitutional
391   cations are also known, but are rare in terms of distribution (<1% of localities).

392   Ni-bearing binary sulfides with 38 structures have been identified among 5,185 localities. Of
393   these species, 10 are Ni-Fe binary sulfides (45% in terms of locality) (Table S1), of which 7 contain Ni
394   and Fe as substitutional cations with an Ni/Fe ratio of 0–35 atomic % being reported [77]. These seven
395   sulfides cover 75% of localities of Ni-Fe binary sulfides with pentlandite ($(Ni,Fe)_9S_8$) being the most
396   prevalent form. The remaining 28 species possess Fe and Ni with fixed stoichiometries (e.g., violarite
397   ($FeNi_2S_4$)), in which Fe and Ni occupy independent crystal lattice sites. The capability of Ni-Fe binary
398   sulfides to have both fixed and varied Ni/Fe ratios in their structures is a unique characteristic
399   different from that of Cu-Fe binary sulfides, in which Cu and Fe tend to form specific structures with
400   fixed stoichiometries.

401 A number of ternary metal sulfides with combinations of Fe–Cu–Ni (seven species), Fe–Cu–Mo
402 (two species; Tarkianite ((Cu,Fe)(Re,Mo)$_4$S$_8$) and Maikainite (Cu$^+_{10}$Fe$^{2+}_3$Mo^{4+}Ge$^{4+}_3$S$^{2-}_{16}$)), and Fe–Cu–W
403 (one species; Ovamboite, Cu$^+_{10}$Fe$^{2+}_3$W^{4+}Ge$^{4+}_3$S$^{2-}_{16}$) have been characterized (Table S2). The occurrence
404 of ternary systems is uncommon (77 localities or 0.05% of the total locality counts of metal sulfides)
405 and it is notable that binary Fe-Mo and Fe-W sulfides are not found in nature, indicating that Cu is
406 important for the incorporation of Mo and W into FeS structures.

3. 4. X-ray amorphous metal sulfides

408 As a clear XRD pattern is required to identify crystal structures, X-ray amorphous species are
409 rarely included in mineralogy databases (Table S3 lists the eight amorphous species recorded in the
410 RRUFF database). Jordisite (MoS$_2$), the second most prevalent Mo single-metal sulfide, is the only
411 amorphous metal sulfide recorded. Using high-resolution transmittance electron microscopy (TEM),
412 jordisite exhibits low crystallinity, but still shows a layered structure with interlayer spacing of ≈ 6 Å
413 resembling that in hexagonal molybdenite (MoS$_2$) [30]. Mo sulfide is also seen in anaerobic sulfidic
414 sediments and basins [26,28,78–80], and its speciation is controlled by the O$_2$ and HS$^-$ concentrations
415 in these environments [26,27]. Mo sulfide associated with Cretaceous deep sea sediments and with
416 other black shales is characterized by the molecular structure of the Mo center coordinated with
417 sulfur and oxygen, as resolved by extended X-ray absorption fine structure spectroscopy [28].
418 Despite of the low number of amorphous species in the database, metal sulfide species with low
419 crystallinity are not rare. Aqueous clusters of FeS, ZnS and CuS constitute a major fraction of the
420 dissolved metal load in anoxic oceanic, sedimentary, freshwater and deep ocean vent environments,
421 and may be possible building blocks during mineral formation [81]. Luther et al. [81] reported that
422 Fe-S, Zn-S, Ag-S clusters with sizes < 3 nm form in the presence of low concentrations (µM order) of
423 metallic ions and sulfides and show remarkable kinetic stability. For example, the half-life of as-
424 formed Ag-S clusters with respect to O$_2$ oxidation is 360 days. In addition, these nanoclusters show a
425 wider band gap in comparison to their bulk counterparts owing to the quantum confinement effect.
426 Cu-S clusters also show wide variation in metal/sulfur stoichiometry (neutral Cu$_3$S$_3$ and anionic Cu$_4$S$_6$
427 clusters). Nanoclusters with varied metal/sulfur stoichiometry are either neutral or negatively
428 charged and are soluble in aqueous solutions. With the advance of atomic resolution structural
429 characterization techniques, such as X-ray absorption spectroscopy and transmittance electron
430 microscopy, low-crystallinity metal sulfide species are expected to be more frequently discovered in
431 geochemical environments. As such amorphous materials adopt a metastable state and have
432 numerous "dangling bonds", the unique band structure and surface properties of X-ray amorphous
433 metal sulfides are expected to have unique catalytic properties in comparison to that of their bulk
434 counterparts.

4. Impact of metal sulfide chemical diversity on catalysis

436 The previous section summarized the marked chemical diversities of natural transition metal
437 sulfides, as exhibited by the large variations in chemical composition, crystal structure and valence
438 states of the component metal and sulfur species. The chemical diversity of metal sulfide minerals
439 partially reflects the "messy" feature of geological environments. In the context of prebiotic chemistry,
440 such diversity among the available catalysts could have generated messy chemistry with an
441 enormous number of possible reactions, leading to the formation of complex prebiotic organic
442 synthesis networks and, ultimately, autocatalytic reaction networks [82,83]. This raises the question
443 of what types of sulfides, or their combinations, could have been involved in prebiotic processes
444 toward the origin of life?
445 To extract valuable information from mineral databases for the screening of prebiotic catalysts,
446 a critical guiding principle is that of "structure-function relationship", including the key reaction
447 intermediate(s) and physicochemical factor(s) dictating catalytic activity. As was introduced in
448 Sections 1 and 2.2, electrocatalytic processes can occur in hydrothermal vent environments for
449 driving prebiotic synthesis. More importantly, the experimental methods and theories developed in
450 the electrocatalysis field can be generally applied for all redox and a portion of non-redox catalytic

451   processes. For instance, redox processes occurring in enzymes have been extensively studied using
452   electrochemical methods [84–86], thereby allowing detailed elucidation of the electron and proton
453   transfer mechanisms. To provide a better understanding of structure-function relationships toward
454   rational catalyst screening, here, we review the electrocatalytic properties of sulfides with well-
455   defined structures that have been extensively studied in engineering fields.

456   *4.1. CO_2 reduction*

457   CO_2 electroreduction has been examined on various types of catalysts, including metals, alloys,
458   metal-organic complexes, homogeneous molecular catalysts, and metal sulfides, in both aqueous
459   solutions and organic solvents [87–90]. The products of these reactions are typically simple C1
460   compounds, such as CO and formate, in water or C2 compounds, such as oxalate, in aprotic solvents
461   [87,88], although Cu was reported to efficiently catalyze CO_2 reduction to hydrocarbons, including
462   methane and ethylene, in water [91,92].
463   Metal sulfides generally exhibit lower catalytic activity for CO_2 reduction than their metal
464   counterparts [12,13,92], but the presence of favorable active sites on metal sulfides is computationally
465   predicted to facilitate the reduction reaction by stabilizing the key reaction intermediates [93]. The
466   edge sites of MoS_2 and Ni-doped MoS_2 preferentially bind COOH* and CHO* to the bridging S atoms
467   and CO* to the metal sites. The binding of intermediates on different sites is expected to decrease the
468   overpotential originating from the intrinsic thermodynamic adsorption energy scaling relations
469   between different intermediates [94,95]. In fact, selective CO_2 electroreduction to CO has been
470   reported on MoS_2 in water containing 4 mol% of an ionic liquid (1-ethyl-3-methylimidazolium
471   tetrafulorobrate; EMIM-BF_4) [96]. CO production occurred at an onset potential as low as 0.054 V (vs.
472   RHE) and the Faraday efficiency increased from <10% to close to 100% by increasing the overpotential
473   from 0.2 to 0.76 V. Notably, no appreciable amount of CO was observed in the absence of ionic liquid.
474   Density functional theory (DFT) calculations suggested that the *d*-orbital electrons of Mo dominating
475   near the Fermi energy level are freely transferred to reactants adsorbed on edge Mo sites. EMIM ions
476   were inferred to stabilize CO_2 via hydrogen bonding to form an [EMIM-CO_2]$^+$ complex and inhibit
477   the conversion of CO_2 to HCO_3^- and CO_3^{2-}. The complexation also lowered the energy barrier for
478   electron transfer from MoS_2 to the physisorbed CO_2 on MoS_2.
479   With the exception of artificial catalytic systems, the mechanistic implications of CO_2 reduction
480   can be obtained from analyzing the catalytic process in biological enzymatic systems. The reversible
481   transformation of CO_2 to CO is catalyzed by a highly asymmetric [$NiFe_4S_4$] cluster in anaerobic carbon
482   monoxide dehydrogenase (CODH), which operates at potentials close to the thermodynamic
483   potential of the CO_2/CO couple (−0.52 V vs. SHE, pH 7) and contains bifunctional metal sites. In Ni-
484   Fe-containing CODH, high-resolution crystallographic structure determination [76] revealed that
485   CO_2 undergoes two-electron reduction after binding to Ni and Fe sites with a μ_2, η^2 mode, and the
486   intermediate with bent-bound CO_2^{2-} is stabilized by substantial π backbonding. The bifunctionality
487   of Ni and Fe to serve as nucleophilic and electrophilic sites, respectively, plays a key role in activating
488   CO_2 and promoting electron transfer from the metal to CO_2. A short length of Ni-C bonds suggests
489   that the Ni center has high nucleophilicity, which likely originates from the integration of Ni into the
490   Fe/S scaffold. Based on these enzymatic properties and mechanisms, sulfide minerals bearing Ni and
491   Fe, which have an Ni site of square planar symmetry and a single unsaturated site, could potentially
492   act as CO_2 reduction catalysts.

493   *4.2. Ammonia synthesis from nitrate/nitrite or nitrogen reduction*

494   Electrochemical ammonia synthesis by nitrate/nitrite reduction was recently studied on
495   synthesized molybdenum and iron sulfides [14,97]. Nitrate and nitrite reduction reactions catalyzed
496   by molybdenum sulfide have evolutionary relevance with respect to enzymatic catalysis, because all
497   nitrate reductase enzymes and one family of nitrite reductases rely on molybdenum-pterin (Mo-S_2)
498   active centers, in which Mo is coordinated by sulfur atoms of a pterin group [98]. He et al. [97] found
499   that product selectivity of nitrite reduction on molybdenum sulfide is pH dependent with respect to
500   the formation of NO, N_2O and NH_4^+. To elucidate the molecular mechanism underlying this

501 selectivity, operando EPR and Raman spectroscopies performed during nitrite reduction revealed
502 that an oxo-ligated Mo(V) species serves as the key intermediates during the selectivity-controlling
503 step [97]. Oxo-ligated Mo(V) species transition from an isotropic to distorted geometry in response
504 to pH change, suggesting that these species decouple electron transfer (ET) from proton transfer (PT).
505 This unique property results in a volcano-type pH-dependent selectivity of N_2O formation, and the
506 optimal pH for this reaction is close to the pKa of Mo^V-oxo species, at which a kinetic balance is
507 anticipated to exist between ET and PT.

508   Nitrogen reduction is another candidate pathway to generate ammonia ($N_2 + 6e^- + 8H^+ \rightarrow$
509 $2NH_4^+$), and several electrocatalytic systems using Fe_2O_3/CNT [99], Fe/CNT [100], and Ru/C [101],
510 among others, as catalysts have been reported to function in aqueous solution at room temperature
511 and ambient pressure. Typically, low Faradaic efficiency (< 1%) was exhibited and H_2 was generated
512 as the main byproduct. The reaction rate was enhanced by increasing the temperature or optimizing
513 the potential. Higher Faradaic efficiencies (4.02%~10.1%) were recently reported by engineering the
514 catalysts [102,103]. For example, through amorphourization of an Au nanocatalyst, structural
515 distortion was observed, which was proposed to increase the concentration of active sites in the
516 catalyst with higher binding affinities towards N_2. To our knowledge, no metal sulfide has been
517 reported to perform electrocatalytic N_2 reduction. As FeMoS cofactor of nitrogenase catalyzes N_2
518 reduction under ambient temperature and pressure, several Mo containing molecular [104,105] and
519 heterogeneous (MoS_2, MoO_3, MoN) [106–108] catalysts have been synthesized for N_2 reduction. For
520 example, Yandulov et al. [104] reported that a Mo triamidoamine complex catalyzes N_2 reduction
521 using decamethyl chromocene and pyridinium salts as electron and proton sources, respectively, at
522 ambient temperature and 1 bar N_2 in an aprotic organic medium. Based on the chemical properties of
523 the isolated intermediates, the reaction is proposed to proceed via a distal associative mechanism,
524 wherein the catalytic intermediates are sequentially protonated and reduced. A single molybdenum
525 center is proposed to function as the active site and cycle from Mo(III) to Mo(VI) states. Note that the
526 displacement of ammonia by dinitrogen is the rate determining step on this molecule catalyst, which
527 differs from heterogeneous Au [102] and MoS_2 [107] catalysts, where the reductive protonation of
528 bound N_2^* is considered to be the rate limiting step based on DFT calculations to weaken the N≡N
529 triple bond.

4.3. Hydrogen evolution and oxidation reactions

531   The H_2 evolution reaction (HER; $2H^+ + 2e^- \rightarrow H_2$ or $2H_2O + 2e^- \rightarrow H_2 + 2OH^-$) has been the most
532 intensively studied electrochemical reaction catalyzed by metal sulfides. As mentioned above, H_2
533 evolution tends to compete with the reduction of N_2, CO_2 and NO_3^- in regions of large overpotential.
534 For this reason, understanding the HER mechanism is expected to aid in the rational design and
535 selection of catalysts and conditions that are selective for N_2, CO_2 and NO_3^- reduction through
536 suppression of HER. HER has been examined on various sulfides, including Fe [109], Co [110], Mo
537 [111–116], and W [117,118] single-metal sulfides, Ni/Fe [119] and Co/Fe [120] binary-metal sulfides,
538 Co-based binary-metal sulfides (with Cu, Ni, Zn) [121], and pyrite-type minerals [122]. Mo sulfide
539 possesses a laminated lattice structure that is highly amenable to electric and structural modifications,
540 and its catalytic property has therefore been investigated in different crystal phases, including
541 hexagonal MoS_2 (2H-MoS_2), chemically exfoliated metallic MoS_2 (1T MoS_2), amorphous MoS_x, Mo-S
542 clusters ($Mo_3S_4^-$), and Mo-Cu binary-metal sulfide (Cu_2MoS_4) [111–116]), and with various degrees of
543 non-stoichiometric defects [113,115], doping [123,124], and hybridization [125–127]. From the results
544 of spectroscopic analyses, including *in situ* and *ex situ* X-ray absorption [128], XPS [129], EPR [130]
545 and Raman spectroscopy [111,130], hexagonal MoS_2 nanoparticles appear to have catalytic activities
546 on edge sites, rather than on basal planes [112,113,130–133]. This possibility has been supported by
547 several experimental studies that have used [Mo-S_2]-bearing compounds, such as [Mo_3S_{13}]$^{2-}$ and
548 [(PY_5Me_2)MoS_2]$^{2+}$, which mimic edge sites [116,133–135].

549   Experimental evidence also suggests that terminal di-sulfur (S-S)$_{tr}$ species are critical for the HER
550 on amorphous MoS_x [111,128,129]. (S-S)$_{tr}$ species provide thermodynamically favorable adsorption
551 sites for hydrogen (Δ_rG^o ~0) by forming unsaturated –S sites through the reductive cleavage of the S-

552   S bond [129,132]. The formation of a molybdenum hydride moiety (Mo-H) also triggers the HER on
553   amorphous MoS_x [130] and on $Mo_3S_4^-$ [136]. Recently, operando Raman spectroscopy revealed a
554   dynamic structural change of a Mo tri-nuclear cluster characterized by Mo-Mo bond weakening and
555   the concurrent emergence of a terminal S-S ligand, indicating that both multinuclear Mo-Mo bonds
556   and terminal S-S ligands play synergistic roles in the HER [137]. A similar mechanism involving
557   exposed disulfur ligands as active sites was proposed to explain the efficient HER that proceeds on
558   amorphous CoS_x [110]. In both WS_2 and MoS_2, the 2H phase material converts into a metallic 1T phase
559   when chemically exfoliated to monolayer thickness. The metallic 1T phase exhibits superior HER
560   activity because of favorable electron transfer rate as well as the thermoneutral adsorption of H [117].
561   Based on these mechanistic studies, sulfides with S_2^{2-} moieties, such as pyrite (FeS_2), marcasite (FeS_2),
562   covellite ($Cu^{+4}Cu^{2+}_2(S_2)_2S_2$), vaesite ($NiS_2$), and cattierite ($CoS_2$), are promising catalysts for H_2
563   evolution owing to the redox activity and suitable adsorption energy of the of S-S species towards
564   H_{ads}.

565   The reverse reaction of the HER, namely the hydrogen oxidation reaction (HOR), is an important
566   half reaction that is predicted to occur at the inner chimney wall-hydrothermal fluid interface of such
567   geoelectrochemical reactors (Figure 1). The HOR supplies most of the reducing electrons for driving
568   reduction reactions at the seawater-mineral interface and is catalyzed efficiently by Pt-group metals,
569   such as Pt, Pd, Ir [138,139] in acidic medium. Moderate HOR catalytic activities have also been shown
570   using Ni-based catalysts, such as Ni [140,141], Ni binary alloys (NiMo, NiTi) [142], and ternary
571   metallic CoNiMo catalyst [143] in alkaline medium, and by Ni complex molecules [144] in organic
572   medium. Based on DFT calculations, the H adsorption energy on the surface dictates the HOR activity.
573   Pt shows thermoneutral adsorption, whereas Ni displays relatively higher adsorption energy
574   (stronger binding). By alloying Ni with other metals, the H binding energy was tuned based on
575   changes to the d-orbitals of Ni, which facilitates the HOR [142,143]. To date, no metal sulfide has been
576   reported to catalyze the HOR, although numerous types of metal sulfides efficiently catalyze the HER,
577   as mentioned above. This contrasts greatly with Fe-S-Ni hydrogenase, which reversibly and
578   efficiently catalyzes both the HER and HOR [86], and is also predicted to thermoneutrally adsorb H
579   based on DFT calculations [132]. Based on Koper's prediction [54], the presence of only one
580   intermediate (generated through an electrochemical step) in a $2e^-/2H^+$ reaction will allow the catalyst
581   to effectively perform both the forward and backward reactions, given that thermoneutral adsorption
582   of the intermediate occurs on the catalyst surface. One possible explanation for the inertness of metal
583   sulfide towards the HOR is that another non-electrochemical step, such as the surface binding of H_2,
584   non-redox dissociation of H-H bond, or deactivation of the catalyst surface, is rate limiting. Because
585   of the importance of the hydrogen oxidation reaction in geoelectrochemical organic synthesis, HOR
586   catalyzed by metal sulfides warrants further investigation.

587   The electrocatalytic studies reviewed above demonstrate that metal sulfides have the potential
588   to function as versatile catalysts for redox reactions that are relevant to prebiotic synthesis. Several
589   key factors of metal sulfide catalysts can be summarized here. First, in-situ spectroscopic analyses
590   have provided insights into the reaction mechanisms of these catalysts and suggest that not only
591   single metal sites, but also heterogeneous surface moieties, such as those with metal-metal, metal-
592   sulfur, metal-hydride, and sulfur-sulfur bonds, play important and occasionally synergistic roles in
593   promoting specific reactions. This is a remarkable feature of metal sulfide catalysts that differs from
594   that observed in metal complex-mediated reaction systems, in which the redox chemistry is mainly
595   dominated by the valence change on single metal centers. Moreover, a surface dominated by metal
596   sites is likely preferable for CO_2 and nitrate electroreduction on metal sulfides, as (di-)sulfur-
597   dominated surface sites will be active for H_2 evolution. Furthermore, the doping of a secondary metal
598   was theoretically predicted to tune the binding energies of the reaction intermediates, such as CHO*,
599   COOH*, and H*, thereby enhancing the CO_2 reduction selectivity by suppressing competing H_2
600   evolution [93]. Therefore, the binary and ternary metal sulfides in the mineralogy database, which
601   includes 193 Cu-bearing binary sulfides species, 38 Ni-bearing sulfide species, and 10 types of ternary
602   metal sulfides, are anticipated to show unique activities in comparison with their single metal sulfide
603   counterparts. The microscopic mechanism of decoupled electron and proton transfer represents a

604   new mechanistic aspect to mutli-electron, multi-proton reactions [53–55] and provides a rational
605   approach to tuning catalytic reactivity and selectivity over wide pH and Eh ranges.

5. Rational screening of metal sulfide catalysts

607   The examples shown in Section 4 highlight the physicochemical factors influencing the catalytic
608   activity of specific types of metal sulfide catalysts. To establish a complex chemical network
609   composed of macromolecules and their building blocks, significant efforts are required to screen and
610   identify efficient mineral catalysts for activating simple molecules (CO_2, N_2, NO_3^-/NO_2^-, H_2, etc.).
611   Although a few prebiotic catalysis studies have attempted to screen metal sulfide catalysts [12,13,51],
612   approaches for rational screening have not yet been described. In this section, we briefly review a
613   theoretical approach for predicting the catalytic activity of electrocatalysts.
614   Electrocatalysis occurs via the adsorption of substrates on active surface site(s), followed by the
615   sequential conversion of the substrates into bound intermediates, and finally, the desorption of
616   products from the catalytic surface. Efficient catalysts are expected to have adsorption energy
617   towards the reactants and bound intermediates that are neither too high nor too low, because too
618   weak binding will not drive effective conversion, whereas too strong binding will lead to the
619   poisoning of active sites (so-called Sabatier principle). Based on this principle, DFT calculations on
620   heterogeneous surfaces developed by Nørskov [94,123,145] highlight the importance of "adsorption
621   energy" as a general descriptor of catalytic activity. This method has been used as a theoretical basis
622   for identifying and designing superior catalysts, and rationalizing structure-function relationships
623   that are experimentally observed [145].
624   DFT has been applied to rationalize the experimentally observed tendency of CO_2
625   electroreduction reactivity on various metal catalysts. Figure 4a-c illustrates typical reaction
626   pathways towards various products, particularly CH_4, CO, $HCOO^-$, CH_3OH, and CH_3CH_2OH, as was
627   summarized by Kortlever et al. [89]. Peterson and Nørskov [94] calculated the CO_2-to-CH_4 reduction
628   pathway on a series of fcc transition metal (211) surfaces and showed that is Cu located at the top of
629   the activity plot and is hence the best catalyst (Figure 4d). On Cu (211), the energetic barrier between
630    $CO_2 \rightarrow COOH^*$ conversion and that of the $CO^* \rightarrow CHO^*$ step was well balanced. The $CO^* \rightarrow CHO^*$
631   process is typically the potential-determining step and leads to a high overpotential (on the order of
632   1 V). The CO_2 reduction pathways towards the products CO, C_2H_4, and CH_3CH_2OH were also
633   calculated on Cu (100) and Cu (211) [146,147]. Generally, negatively charged intermediates, such as
634   the adsorbed $CO_2 \bullet^-$ anion intermediate and adsorbed $(CO)_2^-$ anionic dimer, are critical for C1 and C2
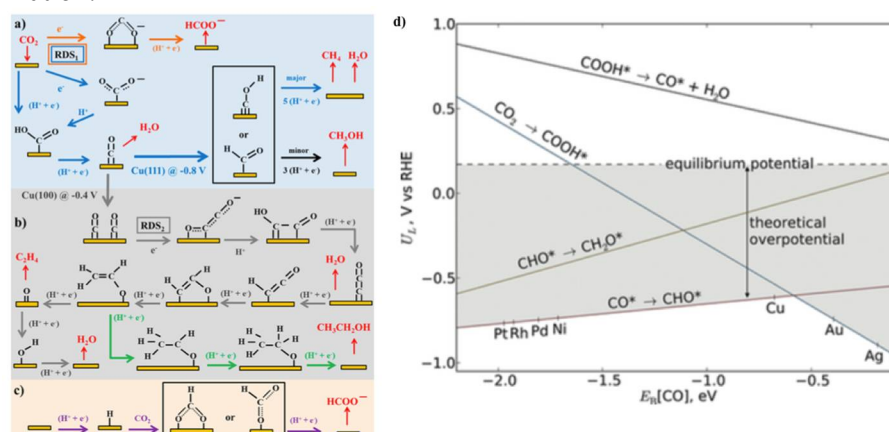635   compound formation.

636

Figure 4. (a-c) Possible reaction pathways for the electrocatalytic reduction of CO_2 to products on
transition metals and molecular catalysts (adapted from ref. [89]): (a) reaction pathways from CO_2 to
CO, CH_4 (blue arrows), CH_3OH (black arrows), and $HCOO^-$ (orange arrows); (b) reaction pathways
from CO_2 to ethylene (gray arrows) and ethanol (green arrows); (c) reaction pathway of CO_2 insertion
into a metal–H bond yielding formate (purple arrows). Species in black are adsorbates, whereas those
in red are reactants or products in solution. Potentials are reported versus RHE, RDS indicates the
rate-determining step, and (H^+ + e^-) indicates steps in which either concerted or separated

proton–electron transfer takes place. (d) Limiting potentials (U_L) for elementary proton-transfer steps in the reduction of CO_2 to CH_4 (adapted from ref. [94]). Each line represents the calculated potential at which the indicated elementary reaction step is neutral with respect to free energy and as a function of the carbon monoxide affinity ($E_B[CO]$) of the electrocatalyst. The theoretical overpotential is defined as the potential difference between the most-negative limiting potential line and the equilibrium potential for the reduction of CO_2 to CH_4 (+0.17 V versus RHE), as highlighted in gray.

Certain alloys facilitate redox reactions with greater efficiencies than the single-metal counterparts, as has been demonstrated for CO oxidation on Pt-alloy, methanation on Fe-Ni alloy, and ethylene oxidation on Ag-alloy [145]. Particularly, CO_2 electroreduction on Cu-Ag alloy shows a higher selectivity for hydrocarbon and oxygenate (ethylene, ethanol, and propanol) formation in comparison with that on Cu [148]. He et al. [149] screened several binary- and ternary-metal alloys (In_xM_{1-x}; M = Fe, Co, Ni, Cu, Zn) for CO_2 reduction to generate CO and found that In_xCu_{1-x} alloys with x = 0.2–0.5 exhibited the highest activity for CO production (90% selectivity). CO evolution on In_xM_{1-x} occurred with the trend Fe < Co < Zn < Ni < Cu, whereas that for H_2 evolution followed the trend Zn < Cu < Ni < Co < Fe. The activity trend for CO formation was consistent with the sequence of CO adsorption energy on the catalyst surfaces calculated by DFT, thus verifying the validity of "CO adsorption energy" as the key descriptor of catalytic activity. In these alloys, the secondary metal changes the average energy of the *d*-electrons (ε_d–ε_F; the *d*-band center with respect to the Fermi level) in the primary metal, resulting in either weaker or enhanced adsorption of key intermediates, thereby potentially facilitating the desired reaction [145]. In addition to CO_2 reduction, DFT calculations based on d-band theory have also been applied for predicting catalytic activity for hydrogen oxidation [138,150,151] and N_2 reduction [152–155].

For reactions involving multiple intermediates, such as CO_2 reduction to CH_4 or alcohols, and N_2 reduction to ammonia, the adsorption energy scaling relationship of chemisorbates commonly leads to intrinsic overpotentials [94,156]. It is possible to lower the onset potential of these reactions through the selective binding of intermediates on different sites or with different binding modes by decoupling the scaling relationship of the binding energies of intermediates [94]. By applying DFT calculations to a mineral with a known crystal structure and chemical composition, the electronic structure of the bulk catalyst and surface sites, including band gap and Fermi levels, can be derived for determining the adsorption energy of key intermediates, which can be used for predicting the activity and identifying superior catalysts (Figure 5). The Materials Project database [157] (https://materialsproject.org/) has been developed for this purpose and is supported by the U.S. Department of Energy (DOE). This database contains the crystal structures of 83,989 inorganic compounds (as of July 31st, 2018). Using high-throughput computing, the band structures of 52,179 compounds have been calculated and can be used for calculating adsorption energy.
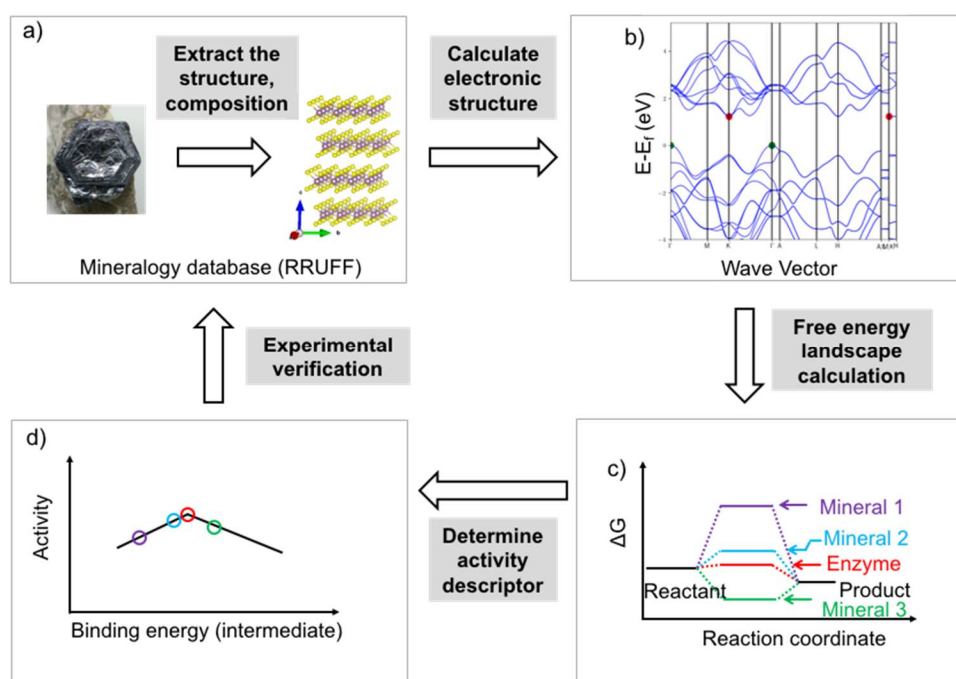
Figure 5. Framework of the methodology proposed for the rational screening of mineral catalysts using DFT calculations. a) Select a series of minerals and extract the structure and chemical composition information from the RRUFF mineralogy database (the mineral shown here is molybdenite, MoS_2, and was obtained from the mindata website: https://www.mindat.org/search.php?name=Molybdenite; the crystal structure was created using BIOVIA Draw software); b) Calculate the electronic structure of the bulk catalyst and surface, and obtain information of the band gap, Fermi level, conductivity, and other electronic properties. The band structure shown here was obtained from the Materials Project database for molybdenite: https://materialsproject.org/; c) Calculate the free energy landscape for the specific reaction (here, the reaction pathway scheme assumes that only one intermediate is involved); d) Determine the activity descriptor (binding energy of the key intermediate). Using this approach, the relative activity profile for a series of minerals can be obtained. The predicted activity profile can be verified using experimental methods to validate the optimized computational model and obtain more precise structure-activity relationships.

Another strategy for exploring catalysts is by referring to biological enzymatic processes. Owing to advances in protein crystallography, high-resolution enzyme structures are becoming increasingly available (e.g., 132,902 protein structures are deposited in the Protein Bank Database as of August 9th, 2018). The Protein Bank Database provides structural information for numerous metal-sulfur enzymes, from which the metal-sulfur distance, sulfur-metal-sulfur angles, and coordination symmetry around the metal center can then be determined. The LUMO and HOMO energy levels of enzyme active centers can be calculated using quantum chemical methods based on simplified enzyme structural models [158,159]. These parameters can be compared with the corresponding crystal structures and band energies of inorganic minerals [69,160,161]. Such comparisons between the electronic structure of minerals and enzymes would aid the screening and identification of suitable mineral catalysts for specific target reactions.

Structure-function relationships can be reliably predicted by combining molecular-level information with quantum chemical calculations. As reviewed in Section 4, heterogeneous sulfide catalysts typically have surface states that are distinct from those of their bulk counterparts and can only be predicted from spectroscopic measurements. In-situ spectroscopic monitoring of the structural evolution of catalysts provides molecular information of key reaction intermediates. The well-defined molecular structure of active species can further be applied in DFT calculations to derive the "descriptor" (adsorption energy of key intermediate) of the activity. This is particularly important in cases where the catalyst structure changes during charge accumulation and/or new intermediate

714 adsorbates are formed. Amorphous materials without easily definable crystal structures are another
715 example of when spectroscopic information is necessary for elucidating reaction mechanisms
716 [111,128,129].

717   Despite these advances in catalytic screening, several challenges remain to be solved in order to
718 effectively apply these approaches. Specifically, for DFT calculations, determining the descriptor in
719 multi–step reactions is more difficult compared to single-step reactions, as the descriptor changes
720 depending on the reaction conditions, such as the atmosphere and solvent composition, pressure, pH,
721 and temperature. The amount of surface coverage by adsorbates and adsorbate-adsorbate
722 interactions also add to the complexity of such computations. In addition, during the reaction process,
723 the original surface structure may be modified. Spectroscopic investigation of the intermediate
724 processes is needed to trace these potential structural changes and provide an accurate molecular
725 basis for DFT calculations.

726 **6. Perspectives**

727   Mineral-mediated catalysis is at the center of chemical evolution involved in the emergence of
728 life. Interdisciplinary knowledge from the fields of catalysis engineering and mineralogy is needed
729 to rationally explore catalytic processes that occur in plausible geochemical settings. The vast
730 chemical diversity of metal sulfide minerals is associated with marked variations in catalytic
731 properties, which are influenced by metal composition, crystal structure, valence state, and defect
732 structure. However, this diversity provides a possible solution to the current problem in prebiotic
733 chemistry that usually an inferior activity, poor selectivity of catalytic process and low chemical
734 diversity among the generated products were shown. As most studies have examined limited types
735 of catalysts, considerable efforts are needed to examine the properties of various types of metal
736 sulfides and their combinations, and determine concrete structure-function relationships that can be
737 used to guide searches of mineralogy databases for target catalysts. Modern computational chemistry
738 and operando spectroscopy approaches are critical for catalysis engineering by establishing the key
739 "descriptor" of activity. Further advances in the understanding of electron and proton transfer and
740 d-band theory, which is generally considered to be the most suitable approach for predicting
741 electrocatalytic performance, will aid in the screening of mineral catalysts for prebiotic synthesis
742 reactions towards understanding the origins of life.

743
744
745
746
747

773

774   **References**

775   1.   Kitadai, N.; Maruyama, S. Origins of building blocks of life: A review. *Geosci. Front.* **2017**,
776   doi:10.1016/j.gsf.2017.07.007.

777   2.   James Cleaves II, H.; Michalkova Scott, A.; Hill, F. C.; Leszczynski, J.; Sahai, N.; Hazen, R. Mineral–
778   organic interfacial processes: potential roles in the origins of life. *Chem. Soc. Rev.* **2012**, *41*, 5502,
779   doi:10.1039/c2cs35112a.

780   3.   Martin, W.; Russell, M. J. On the origin of biochemistry at an alkaline hydrothermal vent. *Philos. Trans.*
781   *R. Soc. Lond. B. Biol. Sci.* **2007**, *362*, 1887–925, doi:10.1098/rstb.2006.1881.

782   4.   Cody, G. D. Geochemical Connections to Primitive Metabolism. *Elements* **2005**, *1*, 139–143,
783   doi:10.2113/gselements.1.3.139.

784   5.   Russell, M. J.; Hall, A. J.; Mellersh, A. R. On the Dissipation of Thermal and Chemical Energies on the
785   Early Earth. In *Natural and Laboratory-Simulated Thermal Geochemical Processes*; Springer Netherlands:
786   Dordrecht, 2003; pp. 325–388 ISBN 978-94-017-0111-2.

787   6.   Wächtershäuser, G. On the Chemistry and Evolution of the Pioneer Organism. *Chem. Biodivers.* **2007**, *4*,
788   584–602, doi:10.1002/cbdv.200790052.

789   7.   Wächtershäuser, G. Before Enzymes and Templates: Theory of Surface Metabolism. *Microbiol. Rev.*
790   **1988**, *52*, 452–484.

791   8.   Russell, M. J.; Hall, A. J. The emergence of life from iron monosulphide bubbles at a submarine
792   hydrothermal redox and pH front. *J. Geol. Soc. London.* **1997**, *154*, 377–402, doi:10.1144/gsjgs.154.3.0377.

793   9.   Russell, M. J.; Hall, A. J. The onset and early evolution of life. In *Memoir 198: Evolution of Early Earth's*
794   *Atmosphere, Hydrosphere, and Biosphere - Constraints from Ore Deposits*; Geological Society of America,
795   2006; Vol. 198, pp. 1–32 ISBN 0072-1069.

796   10.   Lane, N.; Martin, W. F. The origin of membrane bioenergetics. *Cell* **2012**, *151*, 1406–1416,
797   doi:10.1016/j.cell.2012.11.050.

798   11.   Yamamoto, M.; Nakamura, R.; Takai, K. Deep-Sea Hydrothermal Fields as Natural Power Plants.
799   *ChemElectroChem* **2018**, *5*, 1–6, doi:10.1002/celc.201800394.

800   12.   Kitadai, N.; Nakamura, R.; Yamamoto, M.; Takai, K.; Li, Y.; Yamaguchi, A.; Gilbert, A.; Ueno, Y.;
801   Yoshida, N.; Oono, Y. Geoelectrochemical CO production: Implications for the autotrophic origin of
802   life. *Sci. Adv.* **2018**, *4*, eaao7265, doi:10.1126/sciadv.aao7265.

803   13.   Yamaguchi, A.; Yamamoto, M.; Takai, K.; Ishii, T.; Hashimoto, K.; Nakamura, R. Electrochemical CO2
804   Reduction by Ni-containing Iron Sulfides: How Is CO2 Electrochemically Reduced at Bisulfide-Bearing
805   Deep-sea Hydrothermal Precipitates? *Electrochim. Acta* **2014**, *141*, 311–318,
806   doi:10.1016/j.electacta.2014.07.078.

807   14.   Li, Y.; Yamaguchi, A.; Yamamoto, M.; Takai, K.; Nakamura, R. Molybdenum Sulfide: A Bioinspired
808   Electrocatalyst for Dissimilatory Ammonia Synthesis with Geoelectrical Current. *J. Phys. Chem. C* **2017**,
809   *121*, 2154–2164, doi:10.1021/acs.jpcc.6b08343.

810   15.   Nakamura, R.; Takashima, T.; Kato, S.; Takai, K.; Yamamoto, M.; Hashimoto, K. Electrical Current
811   Generation across a Black Smoker Chimney. *Angew. Chemie* **2010**, *122*, 7858–7860,
812   doi:10.1002/ange.201003311.

813   16.   Yamamoto, M.; Nakamura, R.; Oguri, K.; Kawagucci, S.; Suzuki, K.; Hashimoto, K.; Takai, K.
814   Generation of Electricity and Illumination by an Environmental Fuel Cell in Deep-Sea Hydrothermal
815   Vents. *Angew. Chemie* **2013**, *125*, 10958–10961, doi:10.1002/ange.201302704.

816   17.   Barge, L. M.; Kee, T. P.; Doloboff, I. J.; Hampton, J. M. P.; Ismail, M.; Pourkashanian, M.; Zeytounian, J.;
817   Baum, M. M.; Moss, J. a; Lin, C.-K.; Kidd, R. D.; Kanik, I. The fuel cell model of abiogenesis: a new
818   approach to origin-of-life simulations. *Astrobiology* **2014**, *14*, 254–70, doi:10.1089/ast.2014.1140.

819   18.   Barge, L. M.; Branscomb, E.; Brucato, J. R.; Cardoso, S. S. S.; Cartwright, J. H. E.; Danielache, S. O.;
820   Galante, D.; Kee, T. P.; Miguel, Y.; Mojzsis, S.; Robinson, K. J.; Russell, M. J.; Simoncini, E.; Sobron, P.
821   Thermodynamics, Disequilibrium, Evolution: Far-From-Equilibrium Geological and Chemical
822   Considerations for Origin-Of-Life Research. *Orig. Life Evol. Biosph.* **2017**, *47*, 39–56, doi:10.1007/s11084-
823   016-9508-z.

824   19.   Barge, L. M.; Abedian, Y.; Russell, M. J.; Doloboff, I. J.; Cartwright, J. H. E.; Kidd, R. D.; Kanik, I. From
825   Chemical Gardens to Fuel Cells: Generation of Electrical Potential and Current Across Self-Assembling
826   Iron Mineral Membranes. *Angew. Chemie* **2015**, *127*, 8302–8305, doi:10.1002/ange.201501663.

827   20.   Sangster, D. F. Precambrian volcanogenic massive sulfide deposits in Canada: A review. *Geol. Surv.*
828   *Canada Pap.* **1972**, *72–22*, 1–43.

829   21.   Hazen, R. M.; Papineau, D.; Bleeker, W.; Downs, R. T.; Ferry, J. M.; McCoy, T. J.; Sverjensky, D. A.;
830   Yang, H. Mineral evolution. *Am. Mineral.* **2008**, *93*, 1693–1720, doi:10.2138/am.2008.2955.

831   22.   Von Damm, K. Seafloor Hydrothermal Activity: Black Smoker Chemistry And Chimneys. *Annu. Rev.*
832   *Earth Planet. Sci.* **1990**, *18*, 173–204, doi:10.1146/annurev.earth.18.1.173.

833   23.   Reed, M. H. Sulfide Mineral Precipitation from Hydrothermal Fluids. *Rev. Mineral. Geochemistry* **2006**,
834   *61*, 609–631, doi:10.2138/rmg.2006.61.11.

835   24.   Macleod, G.; McKeown, C.; Hall, A. J.; Russell, M. J. Hydrothermal and oceanic pH conditions of
836   possible relevance to the origin of life. *Orig. Life Evol. Biosph.* **1994**, *24*, 19–41, doi:10.1007/BF01582037.

837   25.   Dahl, T. W.; Wirth, S. B. Molybdenum isotope fractionation and speciation in a euxinic lake—Testing
838   ways to discern isotope fractionation processes in a sulfidic setting. *Chem. Geol.* **2017**, *460*, 84–92,
839   doi:10.1016/j.chemgeo.2017.04.018.

840   26.   Helz, G. R.; Bura-Nakić, E.; Mikac, N.; Ciglenečki, I. New model for molybdenum behavior in euxinic
841   waters. *Chem. Geol.* **2011**, *284*, 323–332, doi:10.1016/j.chemgeo.2011.03.012.

842   27.   Erickson, B. E.; Helz, G. R. Molybdenum(VI) speciation in sulfidic waters: stability and lability of
843   thiomolybdates. *Geochim. Cosmochim. Acta* **2000**, *64*, 1149–1158, doi:10.1016/S0016-7037(99)00423-8.

844   28.   Helz, G. R. R.; Miller, C. V. V.; Charnock, J. M. M.; Mosselmans, J. F. W. F. W.; Pattrick, R. A. D. a D.;
845   Garner, C. D. D.; Vaughan, D. J. J. Mechanism of molybdenum removal from the sea and its
846   concentration in black shales: EXAFS evidence. *Geochim. Cosmochim. Acta* **1996**, *60*, 3631–3642,
847   doi:10.1016/0016-7037(96)00195-0.

848   29.   Wilde, P.; Lyons, T. W.; Quinby-Hunt, M. S. Organic carbon proxies in black shales: molybdenum.
849   *Chem. Geol.* **2004**, *206*, 167–176, doi:10.1016/j.chemgeo.2003.12.005.

850   30.   Kao, L. S.; Peacor, D. R.; Coveney, J.; Zhao, G.; Dungey, K. E.; Curtis, M. D.; Penner-Hahn, J. E. A
851   C/MoS2mixed-layer phase (MoSC) occurring in metalliferous black shales from Southern China, and
852   new data on jordisite. *Am. Mineral.* **2001**, *86*, 852–861, doi:10.2138/am-2001-0708.

853   31.   Anbar, A. D. Oceans. Elements and evolution. *Science (80-.).* **2008**, *322*, 1481–3,
854   doi:10.1126/science.1163100.

855   32.   Glass, J. B.; Wolfe-Simon, F.; Anbar, A. D. Coevolution of metal availability and nitrogen assimilation
856   in cyanobacteria and algae. *Geobiology* **2009**, *7*, 100–123, doi:10.1111/j.1472-4669.2009.00190.x.

857   33.   Moore, E. K.; Jelen, B. I.; Giovannelli, D.; Raanan, H.; Falkowski, P. G. Metal availability and the
858   expanding network of microbial metabolisms in the Archaean eon. *Nat. Geosci.* **2017**, *10*, 629–636,
859   doi:10.1038/ngeo3006.

860   34.   Russell, M. J.; Daniel, R. M.; Hall, A. J. On the emergence of life via catalytic iron-sulphide membranes.
861   *Terra Nov.* **1993**, *5*, 343–347.

862   35.   Russell, M. J.; Daia, D. E.; Hall, A. J. The emergence of life from FeS bubbles at alkaline hot springs in
863   an acid ocean. *Thermophiles keys to Mol. Evol. Orig. life* **1998**, 77–126.

864   36.   Roldan, A.; Hollingsworth, N.; Roffey, A.; Islam, H.-U.; Goodall, J. B. M.; Catlow, C. R. A.; Darr, J. A.;
865   Bras, W.; Sankar, G.; Holt, K. B.; Hogarth, G.; de Leeuw, N. H. Bio-inspired CO2 conversion by iron
866   sulfide catalysts under sustainable conditions. *Chem. Commun.* **2015**, *51*, 7501–7504,
867   doi:10.1039/c5cc02078f.

868   37.   Hazen, R. M. Mineral surfaces and the prebiotic selection and organization of biomolecules. *Am.*
869   *Mineral.* **2006**, *91*, 1715–1729, doi:10.2138/am.2006.2289.

870   38.   Orgel, L. E. Polymerization on the rocks: theoretical introduction. *Orig. Life Evol. Biosph.* **1998**, *28*, 227–
871   234, doi:10.1023/A:1006595411403.

872   39.   Shatynski, S. R. The thermochemistry of transition metal sulfides. *Oxid. Met.* **1977**, *11*, 307–320,
873   doi:10.1007/BF00608014.

874   40.   Moh, G. H. High-temperature metal sulfide chemistry. In *Topics in Current Chemistry*; Springer-Verlag:
875   Berlin/Heidelberg, 1978; pp. 107–151 ISBN 978-3-540-35680-6.

876   41.   Chianelli, R. R.; Daage, M.; Ledoux, M. J. Fundamental Studies of Transition-Metal Sulfide Catalytic
877   Materials. *Adv. Catal.* **1994**, *40*, 177–232, doi:10.1016/S0360-0564(08)60658-6.

878   42.   Chianelli, R. R. Periodic trends transition metal sulfide catalysis: Intuition and theory. *Oil Gas Sci.*
879   *Technol.* **2006**, *61*, 503–513, doi:10.2516/ogst:2006022a.

880   43.   Summers, D. P.; Khare, B. Nitrogen Fixation on Early Mars and Other Terrestrial Planets: Experimental
881   Demonstration of Abiotic Fixation Reactions to Nitrite and Nitrate. *Astrobiology* **2007**, *7*, 333–341,
882   doi:10.1089/ast.2006.0032.

883   44.   Summers, D. P. Ammonia Formation By The Reduction Of Nitrite/Nitrate By FeS: Ammonia
884   Formation Under Acidic Conditions. *Orig. Life Evol. Biosph.* **2005**, *35*, 299–312, doi:10.1007/s11084-005-
885   2040-1.

886   45.   Huber, Claudia; Wachterhauser, G. Activated Acetic Acid by Carbon Fixation on (Fe , Ni) S Under
887   Primordial Conditions. *Science (80-.).* **1997**, *276*, 245–247, doi:10.1126/science.276.5310.245.

888   46.   Huber, C.; Wächtershäuser, G. A-Hydroxy and A-Amino Acids Under Possible Hadean, Volcanic
889   Origin-of-Life Conditions. *Science (80-.).* **2006**, *314*, 630–632, doi:10.1126/science.1130895.

890   47.   Huber, C.; Wächtershäuser, G. Peptides by Activation of Amino Acids with CO on (Ni,Fe)S Surfaces:
891   Implications for the Origin of Life. *Science (80-.).* **1998**, *281*, 670–672, doi:10.1126/science.281.5377.670.

892   48.   Huber, C.; Wächtershäuser, G. Primordial reductive amination revisited. *Tetrahedron Lett.* **2003**, *44*,
893   1695–1697, doi:10.1016/S0040-4039(02)02863-0.

894   49.   Hazen, R. M.; Hystad, G.; Golden, J. J.; Hummer, D. R.; Liu, C.; Downs, R. T.; Morrison, S. M.; Ralph, J.;
895   Grew, E. S. Cobalt mineral ecology. *Am. Mineral.* **2017**, *102*, 108–116, doi:10.2138/am-2017-5798.

896   50.   Liu, C.; Hystad, G.; Golden, J. J.; Hummer, D. R.; Downs, R. T.; Morrison, S. M.; Ralph, J. P.; Hazen, R.
897   M. Chromium mineral ecology. *Am. Mineral.* **2017**, *102*, 612–619, doi:10.2138/am-2017-5900.

898   51.   Cody, G. D.; Boctor, N. Z.; Brandes, J. A.; Filley, T. R.; Hazen, R. M.; Yoder, H. S. Assaying the catalytic
899   potential of transition metal sulfides for abiotic carbon fixation. *Geochim. Cosmochim. Acta* **2004**, *68*,
900   2185–2196, doi:10.1016/j.gca.2003.11.020.

901   52.   Roger, I.; Shipman, M. A.; Symes, M. D. Earth-abundant catalysts for electrochemical and
902   photoelectrochemical water splitting. *Nat. Rev. Chem.* **2017**, *1*, 0003, doi:10.1038/s41570-016-0003.

903   53.   Koper, M. T. M. Theory of the transition from sequential to concerted electrochemical proton-electron
904   transfer. *Phys. Chem. Chem. Phys.* **2013**, *15*, 1399–407, doi:10.1039/c2cp42369c.

905   54.   Koper, M. T. M. Theory of multiple proton–electron transfer reactions and its implications for
906   electrocatalysis. *Chem. Sci.* **2013**, *4*, 2710, doi:10.1039/c3sc50205h.

907   55.   Koper, M. T. M. Volcano Activity Relationships for Proton-Coupled Electron Transfer Reactions in
908   Electrocatalysis. *Top. Catal.* **2015**, *58*, 1153–1158, doi:10.1007/s11244-015-0489-3.

909   56.   Nitschke, W.; McGlynn, S. E.; Milner-White, E. J.; Russell, M. J. On the antiquity of metalloenzymes
910   and their substrates in bioenergetics. *Biochim. Biophys. Acta - Bioenerg.* **2013**, *1827*, 871–881,
911   doi:10.1016/j.bbabio.2013.02.008.

912   57.   Russell, M. J.; Barge, L. M.; Bhartia, R.; Bocanegra, D.; Bracher, P. J.; Branscomb, E.; Kidd, R.; McGlynn,
913   S.; Meier, D. H.; Nitschke, W.; Shibuya, T.; Vance, S.; White, L.; Kanik, I. The drive to life on wet and
914   icy worlds. *Astrobiology* **2014**, *14*, 308–43, doi:10.1089/ast.2013.1110.

915   58.   Heinen, W.; Lauwers, A. M. Organic sulfur compounds resulting from the interaction of iron sulfide,
916   hydrogen sulfide and carbon dioxide in an anaerobic aqueous environment. *Orig. Life Evol. Biosph.*
917   **1996**, *26*, 131–150, doi:10.1007/BF01809852.

918   59.   Brandes, J. A.; Boctor, N. Z.; Cody, G. D.; Cooper, B. A.; Hazen, R. M.; Yoder, H. S. Abiotic nitrogen
919   reduction on the early Earth. *Nature* **1998**, *395*, 365–367.

920   60.   Dörr, M.; Käßbohrer, J.; Grunert, R.; Kreisel, G.; Brand, W. A.; Werner, R. A.; Geilmann, H.; Apfel, C.;
921   Robl, C.; Weigand, W. A Possible Prebiotic Formation of Ammonia from Dinitrogen on Iron Sulfide
922   Surfaces. *Angew. Chemie Int. Ed.* **2003**, *42*, 1540–1543, doi:10.1002/anie.200250371.

923   61.   Cody, G. D. Primordial Carbonylated Iron-Sulfur Compounds and the Synthesis of Pyruvate. *Science*
924   *(80-.).* **2000**, *289*, 1337–1340, doi:10.1126/science.289.5483.1337.

925   62.   Booth, B. G.; Chatt, J. The reactions of carbon monoxide and nitric oxide with tertiary phosphine
926   complexes of iron (II), cobalt (II) and nickel (II). *J. Chem. Soc.* **1962**, 2099–2106,
927   doi:10.1039/JR9620002099.

928   63.   Butler, I. S.; Basolo, F.; Pearson, R. G. Kinetics Studies of Carbon Monoxide Insertion Reactions.
929   Reactions of Cyclopentadienyl(methyl)iron Dicarbonyl and Cyclopentadienyl(methyl) Molybdenum
930   Tricarbonyl with Phosphines and Phosphites. *Inorg. Chem.* **1967**, *6*, 2074–2079, doi:10.1021/ic50057a032.

931   64.   Calderazzo, F.; Cotton, F. A. Carbon Monoxide Insertion Reactions. I. The Carbonylation of Methyl
932   Manganese Pentacarbonyl and Decarbonylation of Acetyl Manganese Pentacarbonyl. *Inorg. Chem.*
933   **1962**, *1*, 30–36, doi:10.1021/ic50001a008.

934   65.   Novikov, Y.; Copley, S. D. Reactivity landscape of pyruvate under simulated hydrothermal vent
935   conditions. *Proc. Natl. Acad. Sci.* **2013**, *110*, 13283–13288, doi:10.1073/pnas.1304923110.

936   66.   Ang, R.; Khan, A. U.; Tsujii, N.; Takai, K.; Nakamura, R.; Mori, T. Thermoelectricity Generation and
937   Electron-Magnon Scattering in a Natural Chalcopyrite Mineral from a Deep-Sea Hydrothermal Vent.
938   *Angew. Chem. Int. Ed. Engl.* **2015**, *54*, 12909–12922, doi:10.1002/anie.201505517.

939   67.   Yamaguchi, A.; Li, Y.; Takashima, T.; Hashimoto, K.; Nakamura, R. CO2 Reduction Using an
940   Electrochemical Approach from Chemical, Biological, and Geological Aspects in the Ancient and
941   Modern Earth. In; Springer, Cham, 2016; pp. 213–228.

942   68.   Trail, D.; Watson, E. B.; Tailby, N. D. The oxidation state of Hadean magmas and implications for early
943   Earth's atmosphere. *Nature* **2011**, *480*, 79–82, doi:10.1038/nature10655.

944   69.   Bullett, D. W. Electronic structure of 3d pyrite- and marcasite-type sulphides. *J. Phys. C Solid State Phys.*
945   **1982**, *15*, 6163–6174, doi:10.1088/0022-3719/15/30/010.

946   70.   Uhlig, I.; Szargan, R.; Nesbitt, H. .; Laajalehto, K. Surface states and reactivity of pyrite and marcasite.
947   *Appl. Surf. Sci.* **2001**, *179*, 222–229, doi:10.1016/S0169-4332(01)00283-5.

948   71.   Snowball, I. F. Magnetic hysteresis properties of greigite (Fe3S4) and a new occurrence in Holocene
949   sediments from Swedish Lappland. *Phys. Earth Planet. Inter.* **1991**, *68*, 32–40, doi:10.1016/0031-
950   9201(91)90004-2.

951   72.   Rochette, P.; Fillion, G.; Mattéi, J. L.; Dekkers, M. J. Magnetic transition at 30-34 Kelvin in pyrrhotite:
952   insight into a widespread occurrence of this mineral in rocks. *Earth Planet. Sci. Lett.* **1990**, *98*, 319–328,
953   doi:10.1016/0012-821X(90)90034-U.

954   73.   Boller, H.; IUCr On the synthesis, crystal chemistry and magnetic properties of rasvumite and related
955   compounds. *Acta Crystallogr. Sect. A Found. Crystallogr.* **2004**, *60*, s47–s47,
956   doi:10.1107/S0108767304099088.

957   74.   Silva, J. C. M.; De Abreu, H. a.; Duarte, H. a. Electronic and structural properties of bulk arsenopyrite
958   and its cleavage surfaces – a DFT study. *RSC Adv.* **2015**, *5*, 2013–2023, doi:10.1039/C4RA13807D.

959   75.   Jones, R. A.; Nesbitt, H. W. XPS evidence for Fe and As oxidation states and electronic states in
960   loellingite (FeAs2). *Am. Mineral.* **2002**, *87*, 1692–1698, doi:10.2138/am-2002-11-1219.

961   76.   Fesseler, J.; Jeoung, J. H.; Dobbek, H. How the [NiFe4S4] Cluster of CO Dehydrogenase Activates
962   CO2and NCO-. *Angew. Chemie - Int. Ed.* **2015**, *54*, 8560–8564, doi:10.1002/anie.201501778.

963   77.   van Velzen, A. J.; Dekkers, M. J.; Zijderveld, J. D. A. Magnetic iron-nickel sulphides in the Pliocene and
964   Pleistocene marine marls from the Vrica section (Calabria, Italy). *Earth Planet. Sci. Lett.* **1993**, *115*, 43–55,
965   doi:10.1016/0012-821X(93)90211-Q.

966   78.   Bostick, B. C.; Fendorf, S.; Helz, G. R. Differential adsorption of molybdate and tetrathiomolybdate on
967   pyrite (FeS2). *Environ. Sci. Technol.* **2003**, *37*, 285–291, doi:10.1021/es0257467.

968   79.   Tribovillard, N.; Riboulleau, A.; Lyons, T.; Baudin, F. Enhanced trapping of molybdenum by
969   sulfurized marine organic matter of marine origin in Mesozoic limestones and shales. *Chem. Geol.* **2004**,
970   *213*, 385–401, doi:10.1016/j.chemgeo.2004.08.011.

971   80.   Vorlicek, T. P.; Kahn, M. D.; Kasuya, Y.; Helz, G. R. Capture of molybdenum in pyrite-forming
972   sediments: role of ligand-induced reduction by polysulfides. *Geochim. Cosmochim. Acta* **2004**, *68*, 547–
973   556, doi:10.1016/S0016-7037(03)00444-7.

974   81.   Luther, G. W.; Rickard, D. T. Metal sulfide cluster complexes and their biogeochemical importance in
975   the environment. *J. Nanoparticle Res.* **2005**, *7*, 389–407, doi:10.1007/s11051-005-4272-4.

976   82.   Guttenberg, N.; Virgo, N.; Chandru, K.; Scharf, C.; Mamajanov, I. Bulk measurements of messy
977   chemistries are needed for a theory of the origins of life. *Philos. Trans. A. Math. Phys. Eng. Sci.* **2017**, *375*,
978   20160347, doi:10.1098/rsta.2016.0347.

979   83.   Tawfik, D. S. Messy biology and the origins of evolutionary innovations. *Nat. Chem. Biol.* **2010**, *6*, 692–
980   696, doi:10.1038/nchembio.441.

981   84.   Anderson, L. J.; Richardson, D. J.; Butt, J. N. Catalytic Protein Film Voltammetry from a Respiratory
982   Nitrate Reductase Provides Evidence for Complex Electrochemical Modulation of Enzyme Activity.
983   *Biochemistry* **2001**, *40*, 11294–11307, doi:10.1021/bi002706b.

984   85.   Hirst, J. Elucidating the mechanisms of coupled electron transfer and catalytic reactions by protein film
985   voltammetry. *Biochim. Biophys. Acta* **2006**, *1757*, 225–239, doi:10.1016/j.bbabio.2006.04.002.

986   86.   Hoeben, F. J. M.; Meijer, F. S.; Dekker, C.; Albracht, S. P. J.; Heering, H. A.; Lemay, S. G. Toward
987   Single-Enzyme Molecule Electrochemistry: [NiFe]-Hydrogenase Protein Film Voltammetry at
988   Nanoelectrodes. *ACS Nano* **2008**, *2*, 2497–2504, doi:10.1021/nn800518d.

989   87.   Zhang, W.; Hu, Y.; Ma, L.; Zhu, G.; Wang, Y.; Xue, X.; Chen, R.; Yang, S.; Jin, Z. Progress and
990   Perspective of Electrocatalytic CO 2 Reduction for Renewable Carbonaceous Fuels and Chemicals. *Adv.*
991   *Sci.* **2018**, *5*, 1–24, doi:10.1002/advs.201700275.

992   88.   Costentin, C.; Robert, M.; Savéant, J.-M. Catalysis of the electrochemical reduction of carbon dioxide.
993   *Chem. Soc. Rev.* **2013**, *42*, 2423–2436, doi:10.1039/C2CS35360A.

994   89.   Kortlever, R.; Shen, J.; Schouten, K. J. P.; Calle-Vallejo, F.; Koper, M. T. M. Catalysts and Reaction
995   Pathways for the Electrochemical Reduction of Carbon Dioxide. *J. Phys. Chem. Lett.* **2015**, *6*, 4073–4082,
996   doi:10.1021/acs.jpclett.5b01559.

997   90.   Sakakura, T.; Choi, J.; Yasuda, H. Transformation of Carbon Dioxide Transformation of Carbon
998   Dioxide. *Chem. Rev.* **2007**, *107*, 2365–2387, doi:10.1021/cr068357u.

999   91.   Dinh, C.; Burdyny, T.; Kibria, M. G.; Seifitokaldani, A.; Gabardo, C. M.; García de Arquer, F. P.; Kiani,
1000   A.; Edwards, J. P.; De Luna, P.; Bushuyev, O. S.; Zou, C.; Quintero-Bermudez, R.; Pang, Y.; Sinton, D.;
1001   Sargent, E. H. CO 2 electroreduction to ethylene via hydroxide-mediated copper catalysis at an abrupt
1002   interface. *Science (80-.)*. **2018**, *360*, 783–787, doi:10.1126/science.aas9100.

1003   92.   Hori, Y.; Kikuchi, K.; Suzuki, S. Production of CO and CH4 in electrochemical reduction of CO2 at
1004   metal electrodes in aqueous hydrogencarbonate solution. *Chem. Lett.* **1985**, *14*, 1695–1698,
1005   doi:10.1246/cl.1985.1695.

1006   93.   Chan, K.; Tsai, C.; Hansen, H. A.; Nørskov, J. K. Molybdenum Sulfides and Selenides as Possible
1007   Electrocatalysts for CO 2 Reduction. *ChemCatChem* **2014**, *6*, 1899–1905, doi:10.1002/cctc.201402128.

1008   94.   Peterson, A. A.; Nørskov, J. K. Activity Descriptors for CO 2 Electroreduction to Methane on
1009   Transition-Metal Catalysts. *J. Phys. Chem. Lett.* **2012**, *3*, 251–258, doi:10.1021/jz201461p.

1010   95.   Shi, C.; Hansen, H. A.; Lausche, A. C.; Nørskov, J. K. Trends in electrochemical CO2reduction activity
1011   for open and close-packed metal surfaces. *Phys. Chem. Chem. Phys.* **2014**, *16*, 4720–4727,
1012   doi:10.1039/c3cp54822h.

1013   96.   Asadi, M.; Kumar, B.; Behranginia, A.; Rosen, B. A.; Baskin, A.; Repnin, N.; Pisasale, D.; Phillips, P.;
1014   Zhu, W.; Haasch, R.; Klie, R. F.; Král, P.; Abiade, J.; Salehi-Khojin, A. Robust carbon dioxide reduction
1015   on molybdenum disulphide edges. *Nat. Commun.* **2014**, *5*, 1–8, doi:10.1038/ncomms5470.

1016   97.   He, D.; Li, Y.; Ooka, H.; Go, Y. K.; Jin, F.; Kim, S. H.; Nakamura, R. Selective Electrocatalytic Reduction
1017   of Nitrite to Dinitrogen Based on Decoupled Proton-Electron Transfer. *J. Am. Chem. Soc.* **2018**, *140*,
1018   2012–2015, doi:10.1021/jacs.7b12774.

1019   98.   Maia, L. B.; Moura, J. J. G. How Biology Handles Nitrite. *Chem. Rev.* **2014**, *114*, 5273–5357,
1020   doi:10.1021/cr400518y.

1021   99.   Chen, S.; Perathoner, S.; Ampelli, C.; Mebrahtu, C.; Su, D.; Centi, G. Room-Temperature
1022   Electrocatalytic Synthesis of NH3 from H2O and N2 in a Gas-liquid-Solid Three-Phase Reactor. *ACS*
1023   *Sustain. Chem. Eng.* **2017**, *5*, 7393–7400, doi:10.1021/acssuschemeng.7b01742.

1024   100.   Chen, S.; Perathoner, S.; Ampelli, C.; Mebrahtu, C.; Su, D.; Centi, G. Electrocatalytic Synthesis of
1025   Ammonia at Room Temperature and Atmospheric Pressure from Water and Nitrogen on a Carbon-
1026   Nanotube-Based Electrocatalyst. *Angew. Chemie - Int. Ed.* **2017**, *56*, 2699–2703,
1027   doi:10.1002/anie.201609533.

1028   101.   Kordali, V.; Kyriacou, G.; Lambrou, C. Electrochemical synthesis of ammonia at atmospheric pressure
1029   and low temperature in a solid polymer electrolyte cell. *Chem. Commun.* **2000**, 1673–1674,
1030   doi:10.1039/b004885m.

1031   102.   Bao, D.; Zhang, Q.; Meng, F.-L.; Zhong, H.-X.; Shi, M.-M.; Zhang, Y.; Yan, J.-M.; Jiang, Q.; Zhang, X.-B.
1032   Electrochemical Reduction of N $_2$ under Ambient Conditions for Artificial N $_2$ Fixation and Renewable
1033   Energy Storage Using N $_2$/NH $_3$ Cycle. *Adv. Mater.* **2017**, *29*, 1604799, doi:10.1002/adma.201604799.

1034   103.   Li, S.-J.; Bao, D.; Shi, M.-M.; Wulan, B.-R.; Yan, J.-M.; Jiang, Q. Amorphizing of Au Nanoparticles by
1035   CeO $_x$-RGO Hybrid Support towards Highly Efficient Electrocatalyst for N 2 Reduction under
1036   Ambient Conditions. *Adv. Mater.* **2017**, *29*, 1700001, doi:10.1002/adma.201700001.

1037   104.   Yandulov, D. V. Catalytic Reduction of Dinitrogen to Ammonia at a Single Molybdenum Center.
1038   *Science (80-.).* **2003**, *301*, 76–78, doi:10.1126/science.1085326.

1039   105.   Schrock, R. R. Catalytic reduction of dinitrogen to ammonia at a single molybdenum center. *Acc. Chem.*
1040   *Res.* **2005**, *38*, 955–62, doi:10.1021/ar0501121.

1041   106.   Han, J.; Ji, X.; Ren, X.; Cui, G.; Li, L.; Xie, F.; Wang, H.; Li, B.; Sun, X. MoO $_3$ nanosheets for efficient
1042   electrocatalytic N $_2$ fixation to NH $_3$. *J. Mater. Chem. A* **2018**, *6*, 12974–12977, doi:10.1039/C8TA03974G.

1043   107.   Zhang, L.; Ji, X.; Ren, X.; Ma, Y.; Shi, X.; Tian, Z.; Asiri, A. M.; Chen, L.; Tang, B.; Sun, X.
1044   Electrochemical Ammonia Synthesis via Nitrogen Reduction Reaction on a MoS $_2$ Catalyst: Theoretical
1045   and Experimental Studies. *Adv. Mater.* **2018**, *30*, 1800191, doi:10.1002/adma.201800191.

1046   108.   Zhang, L.; Ji, X.; Ren, X.; Luo, Y.; Shi, X.; Asiri, A. M.; Zheng, B.; Sun, X. Efficient Electrochemical N $_2$
1047   Reduction to NH $_3$ on MoN Nanosheets Array under Ambient Conditions. *ACS Sustain. Chem. Eng.*
1048   **2018**, *6*, 9550–9554, doi:10.1021/acssuschemeng.8b01438.

1049   109.   Di Giovanni, C.; Wang, W. A.; Nowak, S.; Grenèche, J. M.; Lecoq, H.; Mouton, L.; Giraud, M.; Tard, C.
1050   Bioinspired iron sulfide nanoparticles for cheap and long-lived electrocatalytic molecular hydrogen
1051   evolution in neutral water. *ACS Catal.* **2014**, *4*, 681–687, doi:10.1021/cs4011698.

1052   110.   Kornienko, N.; Resasco, J.; Becknell, N.; Jiang, C. M.; Liu, Y. S.; Nie, K.; Sun, X.; Guo, J.; Leone, S. R.;
1053   Yang, P. Operando Spectroscopic Analysis of an Amorphous Cobalt Sulfide Hydrogen Evolution
1054   Electrocatalyst. *J. Am. Chem. Soc.* **2015**, *137*, 7448–7455, doi:10.1021/jacs.5b03545.

1055   111.   Deng, Y.; Ting, L. R. L.; Neo, P. H. L.; Zhang, Y.-J.; Peterson, A. A.; Yeo, B. S. Operando Raman
1056   Spectroscopy of Amorphous Molybdenum Sulfide (MoSx) during the Electrochemical Hydrogen
1057   Evolution Reaction: Identification of Sulfur Atoms as Catalytically Active Sites for H + Reduction. *ACS*
1058   *Catal.* **2016**, *6*, 7790–7798, doi:10.1021/acscatal.6b01848.

1059   112.   Ting, L. R. L.; Deng, Y.; Ma, L.; Zhang, Y.-J.; Peterson, A. A.; Yeo, B. S. Catalytic Activities of Sulfur
1060   Atoms in Amorphous Molybdenum Sulfide for the Electrochemical Hydrogen Evolution Reaction.
1061   *ACS Catal.* **2016**, *6*, 861–867, doi:10.1021/acscatal.5b02369.

1062   113.   Xie, J.; Zhang, H.; Li, S.; Wang, R.; Sun, X.; Zhou, M.; Zhou, J.; Lou, X. W. D.; Xie, Y. Defect-rich MoS2
1063   ultrathin nanosheets with additional active edge sites for enhanced electrocatalytic hydrogen
1064   evolution. *Adv. Mater.* **2013**, *25*, 5807–5820, doi:10.1002/adma.201302685.

1065   114.   Merki, D.; Fierro, S.; Vrubel, H.; Hu, X. Amorphous molybdenum sulfide films as catalysts for
1066   electrochemical hydrogen production in water. *Chem. Sci.* **2011**, *2*, 1262–1267, doi:10.1039/c1sc00117e.

1067 115. Lukowski, M. A.; Daniel, A. S.; Meng, F.; Forticaux, A.; Li, L.; Jin, S. Enhanced Hydrogen Evolution
1068   Catalysis from Enhanced Hydrogen Evolution Catalysis from Chemically Exfoliated Metallic MoS 2
1069   Nanosheets. *J. Am. Chem. Soc.* **2013**, *135*, 10274–10277, doi:10.1021/ja404523s.

1070 116. Jaramillo, T. F.; Bonde, J.; Zhang, J.; Ooi, B. L.; Andersson, K.; Ulstrup, J.; Chorkendorff, I. Hydrogen
1071   evolution on supported incomplete cubane-type [Mo 3S4]4+ electrocatalysts. *J. Phys. Chem. C* **2008**, *112*,
1072   17492–17498, doi:10.1021/jp802695e.

1073 117. Voiry, D.; Yamaguchi, H.; Li, J.; Silva, R.; Alves, D. C. B.; Fujita, T.; Chen, M.; Asefa, T.; Shenoy, V. B.;
1074   Eda, G.; Chhowalla, M. Enhanced catalytic activity in strained chemically exfoliated WS2nanosheets
1075   for hydrogen evolution. *Nat. Mater.* **2013**, *12*, 850–855, doi:10.1038/nmat3700.

1076 118. Yang, J.; Voiry, D.; Ahn, S. J.; Kang, D.; Kim, A. Y.; Chhowalla, M.; Shin, H. S. Two-dimensional hybrid
1077   nanosheets of tungsten disulfide and reduced graphene oxide as catalysts for enhanced hydrogen
1078   evolution. *Angew. Chemie - Int. Ed.* **2013**, *52*, 13751–13754, doi:10.1002/anie.201307475.

1079 119. Long, X.; Li, G.; Wang, Z.; Zhu, H.; Zhang, T.; Xiao, S.; Guo, W.; Yang, S. Metallic Iron–Nickel Sulfide
1080   Ultrathin Nanosheets As a Highly Active Electrocatalyst for Hydrogen Evolution Reaction in Acidic
1081   Media. *J. Am. Chem. Soc.* **2015**, *137*, 11900–11903, doi:10.1021/jacs.5b07728.

1082 120. Wang, D. Y.; Gong, M.; Chou, H. L.; Pan, C. J.; Chen, H. A.; Wu, Y.; Lin, M. C.; Guan, M.; Yang, J.;
1083   Chen, C. W.; Wang, Y. L.; Hwang, B. J.; Chen, C. C.; Dai, H. Highly active and stable hybrid catalyst of
1084   cobalt-doped FeS<inf>2</inf> nanosheets-carbon nanotubes for hydrogen evolution reaction. *J. Am.*
1085   *Chem. Soc.* **2015**, *137*, 1587–1592, doi:10.1021/ja511572q.

1086 121. Huang, Z. F.; Song, J.; Li, K.; Tahir, M.; Wang, Y. T.; Pan, L.; Wang, L.; Zhang, X.; Zou, J. J. Hollow
1087   Cobalt-Based Bimetallic Sulfide Polyhedra for Efficient All-pH-Value Electrochemical and
1088   Photocatalytic Hydrogen Evolution. *J. Am. Chem. Soc.* **2016**, *138*, 1359–1365, doi:10.1021/jacs.5b11986.

1089 122. Faber, M. S.; Lukowski, M. A.; Ding, Q.; Kaiser, N. S.; Jin, S. Earth-abundant metal pyrites (FeS2, CoS2,
1090   NiS2, and their alloys) for highly efficient hydrogen evolution and polysulfide reduction
1091   electrocatalysis. *J. Phys. Chem. C* **2014**, *118*, 21347–21356, doi:10.1021/jp506288w.

1092 123. Tsai, C.; Chan, K.; Nørskov, J. K.; Abild-Pedersen, F. Rational design of MoS 2 catalysts: tuning the
1093   structure and activity via transition metal doping. *Catal. Sci. Technol.* **2015**, *5*, 246–253,
1094   doi:10.1039/C4CY01162G.

1095 124. Xie, J.; Zhang, J.; Li, S.; Grote, F.; Zhang, X.; Zhang, H.; Wang, R. Controllable Disorder Engineering in
1096   Oxygen-Incorporated MoS 2 Ultrathin Nanosheets for Efficient Hydrogen Evolution. *J. Am. Chem. Soc.*
1097   **2013**, *135*, 17881–17888, doi:10.1021/ja408329q.

1098 125. Wang, T.; Zhuo, J.; Du, K.; Chen, B.; Zhu, Z.; Shao, Y.; Li, M. Electrochemically fabricated polypyrrole
1099   and MoSx copolymer films as a highly active hydrogen evolution electrocatalyst. *Adv. Mater.* **2014**, *26*,
1100   3761–3766, doi:10.1002/adma.201400265.

1101 126. Tang, H.; Dou, K.; Kaun, C.; Kuang, Q.; Yang, S. MoSe nanosheets and their graphene hybrids:
1102   synthesis, characterization and hydrogen evolution reaction studies. *Mater. Chem. A* **2014**, *2*, 360–364,
1103   doi:10.1039/c3ta13584e.

1104 127. Li, D. J.; Maiti, U. N.; Lim, J.; Choi, D. S.; Lee, W. J.; Oh, Y.; Lee, G. Y.; Kim, S. O. Molybdenum
1105   sulfide/N-doped CNT forest hybrid catalysts for high-performance hydrogen evolution reaction. *Nano*
1106   *Lett.* **2014**, *14*, 1228–1233, doi:10.1021/nl404108a.

1107 128. Lassalle-Kaiser, B.; Merki, D.; Vrubel, H.; Gul, S.; Yachandra, V. K.; Hu, X.; Yano, J. Evidence from in
1108   Situ X-ray Absorption Spectroscopy for the Involvement of Terminal Disulfide in the Reduction of

1109   Protons by an Amorphous Molybdenum Sulfide Electrocatalyst. *J. Am. Chem. Soc.* **2015**, *137*, 314–321,
1110   doi:10.1021/ja510328m.

1111 129. Casalongue, H. G. S.; Benck, J. D.; Tsai, C.; Karlsson, R. K. B.; Kaya, S.; Ng, M. L.; Pettersson, L. G. M.;
1112   Abild-Pedersen, F.; Nørskov, J. K.; Ogasawara, H.; Jaramillo, T. F.; Nilsson, A. Operando
1113   Characterization of an Amorphous Molybdenum Sulfide Nanoparticle Catalyst during the Hydrogen
1114   Evolution Reaction. *J. Phys. Chem. C* **2014**, *118*, 29252–29259, doi:10.1021/jp505394e.

1115 130. Tran, P. D.; Tran, T. V.; Orio, M.; Torelli, S.; Truong, Q. D.; Nayuki, K.; Sasaki, Y.; Chiam, S. Y.; Yi, R.;
1116   Honma, I.; Barber, J.; Artero, V. Coordination polymer structure and revisited hydrogen evolution
1117   catalytic mechanism for amorphous molybdenum sulfide. *Nat. Mater.* **2016**, *15*, 640–646,
1118   doi:10.1038/nmat4588.

1119 131. Jaramillo, T. F.; Jorgensen, K. P.; Bonde, J.; Nielsen, J. H.; Horch, S.; Chorkendorff, I. Identification of
1120   Active Edge Sites for Electrochemical H2 Evolution from MoS2 Nanocatalysts. *Science* **2007**, *317*, 100–
1121   102, doi:10.1126/science.1141483.

1122 132. Hinnemann, B.; Moses, P. G.; Bonde, J.; Jorgensen, K. P.; Nielsen, J. H.; Horch, S.; Chorkendorff, I.;
1123   Nørskov, J. K. Biomimetic Hydrogen Evolution: MoS2 Nanoparticles as Catalyst for Hydrogen
1124   Evolution. *J. Am. Chem. Soc.* **2005**, *127*, 5308–5309, doi:10.1021/ja0504690.

1125 133. Karunadasa, H. I.; Montalvo, E.; Sun, Y.; Majda, M.; Long, J. R.; Chang, C. J. A Molecular MoS2 Edge
1126   Site Mimic for Catalytic Hydrogen Generation. *Science* **2012**, *335*, 698–702, doi:10.1126/science.1215868.

1127 134. Hijazi, A.; Kemmegne-Mbouguen, J. C.; Floquet, S.; Marrot, J.; Fize, J.; Artero, V.; David, O.; Magnier,
1128   E.; Pegot, B.; Cadot, E. Tuning the electrocatalytic hydrogen evolution reaction promoted by
1129   [Mo2O2S2]-based molybdenum cycles in aqueous medium. *Dalt. Trans* **2013**, *42*, 4848–4858,
1130   doi:10.1039/c2dt32447d.

1131 135. Kibsgaard, J.; Jaramillo, T. F.; Besenbacher, F. Building an appropriate active-site motif into a
1132   hydrogen-evolution catalyst with thiomolybdate [Mo3S13]2- clusters. *Nat. Chem.* **2014**, *6*, 248–253,
1133   doi:10.1038/nchem.1853.

1134 136. Kumar, C. A.; Saha, A.; Raghavachari, K. Bond Activation and Hydrogen Evolution from Water
1135   through Reactions with M 3 S 4 (M = Mo, W) and W 3 S 3 Anionic Clusters. *J. Phys. Chem. A* **2017**, *121*,
1136   1760–1767, doi:10.1021/acs.jpca.6b11879.

1137 137. Li, Y.; Nakamura, R. Structural change of molybdenum sulfide facilitates the electrocatalytic hydrogen
1138   evolution reaction at neutral pH as revealed by in situ Raman spectroscopy. *Chinese J. Catal.* **2018**, *39*,
1139   401–406, doi:10.1016/S1872-2067(17)62945-0.

1140 138. Durst, J.; Siebel, A.; Simon, C.; Hasché, F.; Herranz, J.; Gasteiger, H. A. New insights into the
1141   electrochemical hydrogen oxidation and evolution reaction mechanism. *Energy Environ. Sci.* **2014**, *7*,
1142   2255–2260, doi:10.1039/C4EE00440J.

1143 139. Vasić, D. D.; Pašti, I. A.; Mentus, S. V. DFT study of platinum and palladium overlayers on tungsten
1144   carbide: Structure and electrocatalytic activity toward hydrogen oxidation/evolution reaction. *Int. J.*
1145   *Hydrogen Energy* **2013**, *38*, 5009–5018, doi:10.1016/J.IJHYDENE.2013.02.020.

1146 140. Kiros, Y.; Schwartz, S. Long-term hydrogen oxidation catalysts in alkaline fuel cells. *J. Power Sources*
1147   **2000**, *87*, 101–105, doi:10.1016/S0378-7753(99)00436-X.

1148 141. Zhuang, Z.; Giles, S. A.; Zheng, J.; Jenness, G. R.; Caratzoulas, S.; Vlachos, D. G.; Yan, Y. Nickel
1149   supported on nitrogen-doped carbon nanotubes as hydrogen oxidation reaction catalyst in alkaline
1150   electrolyte. *Nat. Commun.* **2016**, *7*, 10141, doi:10.1038/ncomms10141.

142. Mund, K.; Richter, G.; Sturm, F. von Titanium-Containing Raney Nickel Catalyst for Hydrogen Electrodes in Alkaline Fuel Cell Systems. *J. Electrochem. Soc.* **1977**, *124*, 1, doi:10.1149/1.2133234.

143. Sheng, W.; Bivens, A. P.; Myint, M.; Zhuang, Z.; Forest, R. V.; Fang, Q.; Chen, J. G.; Yan, Y. Non-precious metal electrocatalysts with high activity for hydrogen oxidation reaction in alkaline electrolytes. *Energy Environ. Sci.* **2014**, *7*, 1719–1724, doi:10.1039/C3EE43899F.

144. Wilson, A. D.; Newell, R. H.; McNevin, M. J.; Muckerman, J. T.; Rakowski DuBois, M.; DuBois, D. L. Hydrogen Oxidation and Production Using Nickel-Based Molecular Catalysts with Positioned Proton Relays. *J. Am. Chem. Soc.* **2006**, *128*, 358–366, doi:10.1021/ja056442y.

145. Nørskov, J. K.; Bligaard, T.; Rossmeisl, J.; Christensen, C. H. Towards the computational design of solid catalysts. *Nat Chem* **2009**, *1*, 37–46, doi:10.1038/nchem.121.

146. Montoya, J. H.; Peterson, A. A.; Nørskov, J. K. Insights into C-C Coupling in CO2 Electroreduction on Copper Electrodes. *ChemCatChem* **2013**, *5*, 737–742, doi:10.1002/cctc.201200564.

147. Calle-Vallejo, F.; Koper, M. T. M. Theoretical Considerations on the Electroreduction of CO to C_2 Species on Cu(100) Electrodes. *Angew. Chemie Int. Ed.* **2013**, *52*, 7282–7285, doi:10.1002/anie.201301470.

148. Gurudayal, G.; Bullock, J.; Srankó, D. F.; Towle, C. M.; Lum, Y.; Hettick, M.; Scott, M. C.; Javey, A.; Ager, J. Efficient solar-driven electrochemical CO_2 reduction to hydrocarbons and oxygenates. *Energy Environ. Sci.* **2017**, 2222–2230, doi:10.1039/C7EE01764B.

149. He, J.; Dettelbach, K. E.; Salvatore, D. A.; Li, T.; Berlinguette, C. P. High-Throughput Synthesis of Mixed-Metal Electrocatalysts for CO_2 Reduction. *Angew. Chemie Int. Ed.* **2017**, 1–6, doi:10.1002/anie.201612038.

150. Sheng, W.; Zhuang, Z.; Gao, M.; Zheng, J.; Chen, J. G.; Yan, Y. Correlating hydrogen oxidation and evolution activity on platinum at different pH with measured hydrogen binding energy. *Nat. Commun.* **2015**, *6*, 5848, doi:10.1038/ncomms6848.

151. Skúlason, E.; Tripkovic, V.; Björketun, M. E.; Gudmundsdóttir, S.; Karlberg, G.; Rossmeisl, J.; Bligaard, T.; Jónsson, H.; Nørskov, J. K. Modeling the Electrochemical Hydrogen Oxidation and Evolution Reactions on the Basis of Density Functional Theory Calculations. *J. Phys. Chem. C* **2010**, *114*, 18182–18197, doi:10.1021/jp1048887.

152. Howalt, J. G.; Bligaard, T.; Rossmeisl, J.; Vegge, T. DFT based study of transition metal nano-clusters for electrochemical NH3 production. *Phys. Chem. Chem. Phys.* **2013**, *15*, doi:10.1039/c3cp44641g.

153. Skúlason, E.; Bligaard, T.; Gudmundsdóttir, S.; Studt, F.; Rossmeisl, J.; Abild-Pedersen, F.; Vegge, T.; Jónsson, H.; Nørskov, J. K. A theoretical evaluation of possible transition metal electro-catalysts for N_2 reduction. *Phys. Chem. Chem. Phys.* **2012**, *14*, 1235–1245, doi:10.1039/C1CP22271F.

154. Abghoui, Y.; Garden, A. L.; Hlynsson, V. F.; Björgvinsdóttir, S.; Ólafsdóttir, H.; Skúlason, E. Enabling electrochemical reduction of nitrogen to ammonia at ambient conditions through rational catalyst design. *Phys. Chem. Chem. Phys.* **2015**, *17*, 4909–4918, doi:10.1039/C4CP04838E.

155. van der Ham, C. J. M.; Koper, M. T. M.; Hetterscheid, D. G. H. Challenges in reduction of dinitrogen by proton and electron transfer. *Chem. Soc. Rev.* **2014**, *43*, 5183–91, doi:10.1039/c4cs00085d.

156. Li, H.; Li, Y.; Koper, M. T. M.; Calle-Vallejo, F. Bond-making and breaking between carbon, nitrogen, and oxygen in electrocatalysis. *J. Am. Chem. Soc.* **2014**, *136*, 15694–15701, doi:10.1021/ja508649p.

157. Jain, A.; Ong, S. P.; Hautier, G.; Chen, W.; Richards, W. D.; Dacek, S.; Cholia, S.; Gunter, D.; Skinner, D.; Ceder, G.; Persson, K. A. Commentary: The Materials Project: A materials genome approach to accelerating materials innovation. *APL Mater.* **2013**, *1*, 011002, doi:10.1063/1.4812323.

1193   158.   Dhawan, I. K.; Enemark, J. H. EPR Studies of Oxo–Molybdenum(V) Complexes with Sulfur Donor
1194   Ligands: Implications for the Molybdenum Center of Sulfite Oxidase. *Inorg. Chem.* **1996**, *35*, 4873–4882,
1195   doi:10.1021/IC9605276.

1196   159.   Inscore, F. E.; McNaughton, R.; Westcott, B. L.; Helton, M. E.; Jones, R.; Dhawan, I. K.; Enemark, J. H.;
1197   Kirk, M. L. Spectroscopic Evidence for a Unique Bonding Interaction in Oxo-Molybdenum Dithiolate
1198   Complexes: Implications for σ Electron Transfer Pathways in the Pyranopterin Dithiolate Centers of
1199   Enzymes. *Inorg. Chem.* **1999**, *38*, 1401–1410, doi:10.1021/ic981126o.

1200   160.   Roldan,   a; Santos-Carballal, D.; de Leeuw, N. H. A comparative DFT study of the mechanical and
1201   electronic properties of greigite Fe3S4 and magnetite Fe3O4. *J. Chem. Phys.* **2013**, *138*, 204712,
1202   doi:10.1063/1.4807614.

1203   161.   Vaughan, D. J.; Tossell, J. A. Electronic structures of sulfide minerals - Theory and experiment. *Phys.*
1204   *Chem. Miner.* **1983**, *9*, 253–262, doi:10.1007/BF00309575.

1205